SIGNAL PROCESSING METHODS TO QUANTIFY SCATTERING OF ANGLE-BEAM SHEAR WAVES FROM THROUGH-HOLES IN PLATES

A Thesis
Presented to
The Academic Faculty

by

Joseph W. Kummer

In Partial Fulfillment
Of the Requirements for the Degree
Master of Science in the
School of Electrical and Computer Engineering

Georgia Institute of Technology
December 2015

SIGNAL PROCESSING METHODS TO QUANTIFY SCATTERING OF ANGLE-BEAM SHEAR WAVES FROM THROUGH-HOLES IN PLATES

Approved by:

Dr. Jennifer E. Michaels, Advisor
School of Electrical and Computer Engineering
Georgia Institute of Technology

Dr. Thomas E. Michaels
School of Electrical and Computer Engineering
Georgia Institute of Technology

Dr. Thomas K. Gaylord
School of Electrical and Computer Engineering
Georgia Institute of Technology

Date Approved: 2 December 2015

Let the future tell the truth, and evaluate each one according to his work and accomplishments. The present is theirs; the future, for which I have really worked, is mine.

- Nikola Tesla

To my family,

Mike, Maureen, Steven, James, and Monica,

for their support throughout my academic career.

ACKNOWLEDGEMENTS

I would like to thank my advisor, Dr. Jennifer Michaels, for her guidance throughout this research. Her dedication to teaching and support for her students has made my experience in the QUEST Lab very enjoyable. She has significantly influenced my development as a researcher and taught me countless lessons that extend beyond the laboratory and into all aspects of my life.

I would also like to thank the other members of my committee, Dr. Thomas Michaels and Dr. Thomas Gaylord. I am especially grateful to Dr. Gaylord for his support throughout my academic career and for offering me an opportunity to work in the Optics Lab as an undergraduate. His enthusiasm for research and teaching, both in and out of the classroom, has inspired me to pursue lofty goals. I consider him one of my greatest influences as a student at Georgia Tech.

Thank you to my friends and colleagues in both the QUEST and Optics Labs for their insight, support, and company. I would also like to thank all of my friends, peers, and professors at the Georgia Institute of Technology, from whom in the past six years I have learned to become a *helluva* engineer.

To my family, their love and support throughout my life has made me the person I am today. I owe my greatest gratitude to my parents, Mike and Maureen, brothers, Steven and James, and girlfriend, Monica. They have all had an immeasurable impact on my life and I look forward beginning the next chapter of my life with them.

This project was funded by the Air Force Research Laboratory (AFRL) under Contract No. FA8650-10-D-5210.

TABLE OF CONTENTS

LIST OF TABLES

LIST OF FIGURES

SUMMARY

The objective of this thesis is to develop, describe and demonstrate analysis techniques that quantify the scattering of angle-beam ultrasonic waves from through-holes in plates. This topic is of interest because increased understanding of the scattering of ultrasonic waves is important for the development of many nondestructive evaluation (NDE) applications. Angle-beam techniques are commonly used in industry to detect and characterize defects, and many structures of concern have plate-like components. Scattering from through-holes is particularly important because cracks tend to form around fastener holes, which have high stress concentrations. In addition, varying boundary conditions within a fastener hole can change over the course of a structure's lifetime and may have significant effects on NDE results.

Experimental procedures for acquiring wavefields, which measure the out-of-plane motion of ultrasonic waves on the surface of a specimen and allow for the visualization and characterization of propagating waves, are presented. Wavefields are obtained for through-holes with a variety of fill conditions, including epoxy and complete and partial filling with metal inserts to investigate the effects of boundary conditions on ultrasonic scattering.

Methods are described for obtaining radial and directional energy maps, each of which quantify scattering as a function of scattered angle and phase velocity. Both methods use frequency-wavenumber analysis to obtain scattering information, but differ in the nature of the information obtained from their respective energy maps. For both methods, baseline subtraction of energy maps is used to obtain scattering patterns, which

quantify the contribution of each wave mode present in the scattered wavefield as a function of scattered angle.

Each method is demonstrated in the analysis of data from a series of experiments that consider a through-hole with varying fill conditions. The results show that both of the methods developed in this thesis provide useful scattering information and offer metrics for comparing incremental scattering scenarios. Particularly for the characterization of scattering from through-holes in plates, the directional energy mapping method emerges as a more promising technique because it mitigates the effects of incident waves more effectively than the radial energy mapping method. Although the methods for generating radial and directional energy maps are applied to angle-beam wavefield measurements, the techniques presented in this thesis are generally applicable to any set of wavefield data containing a scatterer of interest.

CHAPTER 1

INTRODUCTION

The purpose of this thesis is to develop signal processing techniques to quantify ultrasonic scattering of angle-beam shear waves from through-holes in plates. This chapter presents a brief background describing the importance of understanding ultrasonic scattering from defects and the factors motivating this research. Next, research goals are outlined, which focus on the development of new methods for estimating scattering of angle-beam waves using wavefield imaging. Particular attention is paid to understanding scattering from through-holes and quantifying the effects of through-hole fill conditions. Finally, the structure of the remaining chapters of this thesis is summarized.

1.1 Background and Motivation

Ultrasonic nondestructive evaluation (NDE) refers to a wide range of techniques to characterize material properties and defects [1]. Ultrasonic NDE has been adopted as a reliable maintenance and diagnostic tool in a wide range of industries. For example, regular inspection of aircraft components of both military and civilian aircraft is required to ensure safe and reliable operation. Ultrasonic NDE methods are an integral part of the maintenance of aircraft and are used to detect structural flaws that would likely cause part failure before the next maintenance period. The scattering of ultrasonic waves by both defects and structural features has been the topic of extensive research because the reliability and accuracy of ultrasonic NDE applications can benefit from an increased understanding of the interaction of waves with scatterers of interest.

Through-holes in plates are of particular interest because many engineered structures of concern to industries employing NDE contain plate-like components. In addition, through-holes mimic fastener holes, which tend to be areas of high stress concentration and the site of crack origination and growth. Angle-beam NDE, which utilizes a piezoelectric transducer and angled acrylic wedge to generate off-normal ultrasonic bulk waves in a specimen, is a common method used in industry for ultrasonic flaw detection because such bulk waves, which propagate within the object of interest, allow access to subsurface features. Wavefield imaging, which is a technique used to measure the out-of-plane motion of ultrasonic waves on the surface of a specimen and allows for the visualization and characterization of propagating waves, is a viable option for studying angle-beam ultrasonic scattering from through-holes in plates.

1.2 Research Goals and Contributions

The main goal of this research is to develop and implement methods for the analysis of ultrasonic scattering from through-holes in plates. The information gained from the application of these methods provides a better understanding of the interaction of ultrasonic waves with defects, which may be used to improve ultrasonic NDE methods. In this thesis, two methods are introduced to obtain scattering information directly from wavefield measurements of angle-beam bulk waves, although the techniques may be applied to any 3-D wavefield measurements. These two methods are applied to through-holes with various fill conditions to test their effectiveness and to investigate the effects of boundary conditions on ultrasonic scattering.

1.3 Thesis Organization

The remainder of this thesis is organized as follows: Chapter 2 introduces the main topics pertinent to this research in more detail and provides a literature review of previous research efforts in the areas of angle-beam NDE, acoustic wavefield imaging and the quantification of ultrasonic scattering. Research objectives are presented and put into context with prior research. In Chapter 3, experimental procedures for measuring wavefields are described and a summary of experiments considering the effects of fill condition on ultrasonic scattering is presented. Wavefield time snapshots are shown and important features of a wavefield are described to motivate the need for signal processing techniques that utilize wavefield imaging to experimentally measure ultrasonic scattering. Chapters 4 and 5 introduce two techniques for analyzing wavefields to obtain scattering patterns. Both methods utilize interpolation and multi-dimensional Fourier transforms to estimate scattering from a through-hole. Each technique is demonstrated by processing wavefields for a variety of fill conditions. A comparison of the two signal processing methods, discussing the strengths and weaknesses of each approach, is provided in Chapter 6 and concluding remarks, including recommendations for future work, are offered in Chapter 7.

CHAPTER 2

LITERATURE REVIEW

The purpose of this chapter is to introduce and discuss previous research efforts related to angle-beam ultrasonic testing, wavefield imaging, and analysis techniques for quantifying scattering of ultrasonic waves in plates. This chapter includes a brief summary of the fundamental equations governing ultrasonic wave propagation and describes the types of waves that may exist in plate-like structures. Nondestructive evaluation (NDE) is defined and summarized with a focus on ultrasonic NDE, and angle-beam testing in particular. Acoustic wavefield imaging is presented as an effective experimental tool for understanding wave propagation and the interaction of waves with defects, and a review of research efforts to analyze ultrasonic scattering is provided. Finally, the work in this thesis is put into context in relation to the previous work detailed in the literature review and the research objectives of this thesis are outlined.

2.1 Ultrasonic Wave Propagation

The theory of ultrasonic wave propagation in solids was developed in the late nineteenth century for homogenous, isotropic, infinite, elastic solids, which resulted in a mathematical representation of mechanical waves in solid media [1]. The work of Rayleigh [2] and Lamb [3] provide a basis for the understanding of wave propagation in both infinite and bounded elastic solids; the knowledge gained from their work forms the basis of many ultrasonic NDE methods.

2.1.1 Elastic Wave Equation

The propagation of ultrasonic waves in elastic solids is governed by a single equation, which allows for the propagation of longitudinal waves, where particle motion is parallel to the direction of propagation, and shear waves, where particle motion is transverse to the wave's propagation direction. Particle displacement of a propagating elastic wave is expressed by a three-dimensional vector,

$$\mathbf{u} = \begin{bmatrix} u_x(x, y, z, t) \\ u_y(x, y, z, t) \\ u_z(x, y, z, t) \end{bmatrix}, \tag{2.1}$$

where u_x, u_y, and u_z are the particle displacement in the x, y, and z directions, respectively, and are a function of three-dimensional space (x, y, z) and time t.

In a linear, homogenous, isotropic elastic medium, particle displacement of a propagating elastic wave obeys the elastic wave equation,

$$\frac{\partial^2 \mathbf{u}}{\partial t^2} = c_l{}^2 \nabla\nabla\cdot\mathbf{u} - c_s{}^2 \nabla\times\nabla\times\mathbf{u}, \tag{2.2}$$

where $\mathbf{u}$ is the three-dimensional displacement vector and c_l and c_s are the propagation velocities of longitudinal and shear waves, respectively, defined as

$$c_l = \sqrt{\frac{\lambda + 2\mu}{\rho}} \tag{2.3}$$

and

$$c_s = \sqrt{\frac{\mu}{\rho}}, \tag{2.4}$$

where μ and λ are the Lamè constants, which describe the linear stress-strain relation in an isotropic solid.

A plane wave is one possible solution to the elastic wave equation given in Eq. (2.2), where the displacement, $\vec{u}$, is only a function of the direction of wave propagation. The displacement can be expressed as

$$\vec{u}(\vec{x},t) = \vec{A}\cos(\omega t - \vec{k}\cdot\vec{x}), \tag{2.5}$$

where ω is the angular frequency and $\vec{k}$ is the wavenumber [4], which can be expressed as a vector of the form

$$\vec{k} = \begin{bmatrix} k_x \\ k_y \\ k_z \end{bmatrix}. \tag{2.6}$$

The wavenumber is related to the angular frequency, ω, and phase velocity, c, of a propagating wave by

$$|k| = \frac{\omega}{c}, \tag{2.7}$$

where the angular frequency is related to the temporal frequency, f, by

$$\omega = 2\pi f \tag{2.8}$$

and c is equal to c_l or c_s for a propagating longitudinal or shear wave, respectively. The frequency and wavenumber provide valuable information about the direction, wavelength, and velocity of a propagating wave, which is exploited in analysis techniques to quantify ultrasonic wave scattering.

The propagation characteristics of reflected and transmitted elastic waves at an interface are described in detail by Shull [1], and are complicated by the existence of two bulk wave modes and the properties of the two media. In general, since elastic waves can propagate as either a longitudinal or shear mode, two reflected and two refracted waves are potentially generated as a result of the interaction of an incident elastic wave with an

interface. In addition, two critical angles exist for longitudinal and shear modes, respectively, which cause refracted waves to travel along the boundary of the interface.

2.1.2 Types of Ultrasonic Waves in Plates

The previous discussion of the elastic wave equation describes the propagation of bulk waves, where the wavelength of the propagating wave is small relative to the thickness of the medium. As mentioned previously, there are two types of bulk wave modes: longitudinal, with particle motion parallel to the direction of propagation, and shear, with particle motion perpendicular to the direction of propagation. The velocities of longitudinal and shear waves depend on the properties of the material, given in Eq. (2.3) and Eq. (2.4). The propagation directions and velocities of bulk waves in plates are defined by their frequency and wavenumber, and reflection, refraction, and mode conversion of bulk waves are governed by Snell's Law [1].

Guided waves form as a result of the interaction of bulk waves at a material boundary and are categorized by the interface that generates them. Rayleigh waves are a type of guided wave that can form when a bulk wave is critically refracted and travels along the boundary of a solid-vacuum interface. They have elliptical particle motion and propagate at a velocity, c_r, approximated by

$$c_r = \frac{0.87 + 1.12\nu}{1+\nu} c_s , \tag{2.9}$$

where ν is the Poisson's ratio and c_s is the velocity of shear waves for a particular material [1]. Lamb waves are another type of guided wave that propagates through the thickness of a finite, single-layer plate. They form as bulk and evanescent waves reflect, mode convert, and interact at each surface of the plate, interfering with each other to

create resonant waves that may be either symmetric or antisymmetric about the center of the plate. The velocity of a Lamb wave is dependent on the frequency and symmetry of the wave and the thickness and material properties of the plate [1]. The wavelength of Lamb waves are of the same order of magnitude as the plate thickness and become Rayleigh waves at high frequencies.

2.2 Nondestructive Evaluation

According to the American Society of Nondestructive Testing, "[n]ondestructive evaluation (NDE) is the examination of an object with technology that does not affect the object's future usefulness" [1]. The goal of NDE is to determine the quality and integrity of a specimen without damaging the object. NDE is employed as an inspection method for economic and safety reasons and can be used for quality control purposes in a manufacturing setting or as a maintenance and diagnostic tool, among many other applications. A variety of techniques are used for NDE applications depending on the characteristics of the object of interest and the nature of the expected defect. The most commonly used test methods are ultrasonic testing, radiographic testing, electromagnetic testing, magnetic particle testing, liquid penetrant testing, vibration analysis, and visual inspection [5]. Ultrasonic NDE is a robust technique that allows for subsurface inspection and can be applied to a wide range of materials and industries, making it one of the most widely used methods today [1]. This section provides a summary of ultrasonic NDE methods with a focus on angle-beam NDE.

2.2.1 Ultrasonic NDE

Ultrasonic NDE methods are widely used to characterize material properties and to detect and classify defects for a wide range of applications in aircraft, transportation,

infrastructure, medical, manufacturing and other industries [1,6]. In ultrasonic testing, a transducer is used to convert an electrical signal into mechanical vibrations, which results in a propagating ultrasonic wave. Pitch-catch methods, where two separate transducers are used to transmit and receive, and pulse-echo methods, where the transducer acts as both the transmitter and receiver, are used to measure the wave's response to the geometry and properties of the object of interest [1]. These methods depend on the nature of elastic wave propagation in solids to obtain information about defects.

2.2.2 Angle-Beam NDE

Angle-beam ultrasonic testing utilizes an angled wedge to inject bulk waves into a specimen at an angle and is a technique commonly used in industry for ultrasonic flaw detection. An angle-beam probe consists of an acrylic wedge and piezoelectric transducer; an ultrasonic couplant is used to couple energy across the transducer-wedge and wedge-specimen interfaces. The transducer generates a longitudinal mode within the wedge, which may produce longitudinal and shear modes within the specimen through refraction and mode conversion. However, the angle of the wedge is typically chosen to produce incident longitudinal waves at an angle greater than the first critical angle such that only shear waves are transmitted into the test specimen. The most commonly used angle beam probes are designed to produce shear waves at 45º, 60º, or 70º in steel [6].

In plates, angle-beam bulk waves propagate within the medium and reflect between the two surfaces of the plate in a series of V-paths or skips, where a single skip refers to a sound path starting at the top surface, reflecting from the bottom surface, and returning to the top surface [7]. Because of the nature of bulk wave propagation within a plate, angle-beam testing allows for subsurface defect detection and material

characterization, is commonly used for weld inspection [6], and has been used to characterize plates with surface breaking cracks [8], rough crack-like defects [9], and cracks originating from fastener holes [10].

2.3 Acoustic Wavefield Imaging

Acoustic wavefield imaging allows for the visualization of waves propagating from a fixed source and their subsequent interaction with defects and structural features. Developments in measurement technology have made wavefield imaging an effective procedure for damage detection and characterization, as well as for validation of numerical modeling and simulation efforts [11]. In this section, methods for measuring and analyzing wavefields are summarized, including a discussion of common formats for presenting and analyzing ultrasonic data and a brief summary of multi-dimensional Fourier transforms.

2.3.1 Measurement Methods

Acoustic wavefields are typically measured by mechanically scanning a laser Doppler vibrometer (LDV) or air-coupled ultrasonic transducer (AUT) over a two-dimensional rectilinear grid to record the surface motion generated from an attached piezoelectric transducer. Both LDV and AUT systems have been successfully demonstrated for recording the wavefields of bulk waves [7] and guided waves [12], respectively. There are many more published results for wavefield imaging using guided waves than for bulk waves, likely because of the higher temporal and spatial bandwidth requirements for bulk wave measurements at typical frequencies used for NDE. Wavefield measurements in the 1-10 MHz range include surface waves generated by a

pulsed infrared laser [13], bulk wave propagation in pipes and blocks [14] and surface acoustic waves reflecting from a complex, surface-breaking crack [15].

2.3.2 Formatting Wavefield Data

Ultrasonic data are commonly presented in three formats: A-scans, B-scans, and C-scans [16]. In this thesis, wavefield data are defined as a three-dimensional function, $w(x,y,t)$, describing the out-of-plane surface motion of ultrasonic waves propagating within a scan area at spatial location (x,y) and time t. Since the presentation formats are obtained from wavefield data, the conventions used here are slightly different than their traditional definitions in ultrasonic testing [17].

In this thesis, an A-scan is a one-dimensional signal, $f(t)$, which is obtained by observing the surface displacement at a single spatial location within the wavefield as a function of time. Similarly, a B-scan is a two-dimensional signal, $f(r,t)$, composed of a series of A-scans obtained along a prescribed path, where r defines the distance along the length of an arbitrary B-scan path. From the wavefield data, a B-scan is obtained by extracting the received signal as a function of time at each spatial location along the B-scan path, which is typically a straight line. Finally, a C-scan, $f(x,y)$, as defined in this research, is a two-dimensional function obtained from the wavefield, over the entire scan area. A C-scan may be defined as the energy at each spatial location in the scanned area over a length of time or as an image of the wavefield at a single time sample, which is referred to as a time snapshot in the following chapters.

2.3.3 Frequency-Wavenumber Analysis

Frequency-wavenumber analysis is a common technique used in a variety of signal processing applications, and is particularly useful for identifying propagating wave

modes from wavefield data [7]. In general, a multi-dimensional Fourier transform is used to transform a function in the space-time domain, $f(x,y,z,t)$, into a function in the frequency-wavenumber domain, $F(k_x,k_y,k_z,\omega)$, although the number of dimensions can be constrained to fit the dimensionality of any of the ultrasonic data formats described previously. The 3-D Fourier transform, $W(k_x,k_y,\omega)$, of a wavefield, $w(x,y,t)$, is found by

$$W(k_x, k_y, \omega) = \int\int\int w(x, y, t) e^{-j(\omega t - k_x x - k_y y)} dx dy dt \,, \qquad (2.10)$$

where k_x and k_y are the wavenumber components in the x and y directions and ω is the angular frequency. The Fourier transform of a B-scan can be found in a similar way by restricting the dimensions to r and t, resulting in data as a function of k_r and ω.

A variety of processing techniques have been developed to analyze wavefield measurements in the frequency-wavenumber domain. Local wavenumber estimation techniques have been used for defect detection [18] and characterization [19] in composite plates and estimation of Lamb wave dispersion curves [20]. Ruzzene [21] utilized filtering in the frequency-wavenumber domain to decompose the wavefield into incident and reflected waves to enhance defect detection and remove incident wave contributions. In both guided and bulk wave applications, the wavefield typically contains multiple modes, which can be identified using multi-dimensional Fourier transforms. Filtering techniques have been used to separate guided wave modes [11,22], allowing for independent analysis of each mode in the time-space domain.

2.4 Ultrasonic Scattering

The scattering of ultrasonic waves by both defects and structural features has been the topic of extensive research since the reliability and accuracy of NDE applications can benefit from an increased understanding of the interaction of ultrasonic waves with

scatterers of interest. Scattering information for both guided and bulk waves has been obtained through analytical, numerical modeling, and experimental techniques. However, many scattering studies primarily utilize analytical or numerical modeling methods to obtain information about particular defect geometries.

Scattering behavior in the form of transmission and reflection coefficients has been obtained for guided Lamb wave scattering from strip welds [23], rivet holes with edge cracks [24], adhesively bonded joints [25, 26], and through-thickness cracks [27]. Lamb wave scattering behavior in the form of scattering patterns and scattering matrices has been obtained from models and experiments for through-holes [28,29], notches and cracks [30], and crack-like defects emanating from through-holes [31]. In experimental setups, Lamb wave scattering information was obtained by utilizing an array of discrete transducers to measure transmission and reflection coefficients between a limited number of pitch-catch transducer pairs [27,31].

Bulk wave scattering efforts have primarily utilized analytical and numerical modeling techniques because of the bandwidth requirements of experimental bulk wave measurement. Analytical models have been developed to characterize scattered bulk waves for scatterers with relatively simple geometries including planar surface breaking cracks [32] and cylindrical cavities [33,34]. Other methods have modeled elastic wave scattering using direct numerical approaches to produce scattering patterns from spherical [35] and cylindrical cavities [35,36] in bulk media and rough crack-like defects [9]. Similarly, bulk wave scattering matrices have been obtained from models and experiments using ultrasonic array processing techniques for through-thickness holes and slots [37], fatigue cracks, and welds with artificial welded-in defects [38].

2.5 Research Objectives and Context

The objective of this work is to develop signal processing methods to quantify scattering of angle-beam shear waves from through-holes in plates using experimentally acquired wavefield measurements. As summarized previously, bulk wave scattering research has been limited predominantly to analytical and modeling approaches. However, advances in wavefield imaging have allowed for reliable acquisition of bulk wavefields [17]. This thesis aims to develop novel techniques to quantify experimental bulk wave scattering from through-holes in plates and study the effects of changing through-hole fill conditions. This topic is of interest because angle-beam techniques are commonly used in industry to characterize material properties and defects, and many structures of concern have plate-like components. Scattering from through-holes is particularly important because cracks tend to form around fastener holes, which have high stress concentrations. In addition, varying boundary conditions within a fastener hole can change over the course of a structure's lifetime and may have significant effects on NDE results.

Two methods are presented to study the scattering of ultrasonic waves from through-holes with various fill conditions. Scattering patterns are obtained for both methods to quantify scattering as a function of polar angle and wave mode. Scattering is measured for a variety of fill conditions, including epoxy and complete and partial filling with aluminum and steel inserts. Experimental results are presented to demonstrate the utility of these techniques for quantifying angle-beam bulk wave scattering from through-holes.

CHAPTER 3

EXPERIMENTAL PROCEDURES

This chapter describes the experimental setup and procedures used to acquire angle-beam wavefield measurements, and provides a summary of experiments, which details the experimental wavefield measurements used throughout this research. A series of time snapshots are shown to illustrate the nature of the acquired experimental data and provide context to understand the signal processing methods described in this thesis.

3.1 Experimental Setup

A scanning laser Doppler vibrometer (SLDV) system was utilized to measure wavefield data on the surface of a mirror-finish, 305 mm × 305 mm × 6.35 mm thick aluminum plate using experimental procedures similar to those used previously by Dawson [7,17].

A 1-10 MHz linear chirp excitation of length 180 μs and amplitude of 200 Vpp was produced with an Agilent 33250A function generator and Ritec RAM-5000 amplifier. Waves were generated in the plate using an angle-beam probe consisting of a 5 MHz Panametrics C543 transducer and Olympus ABWM-4T-60 angle wedge. The wedge was designed to generate shear vertical waves with a refracted angle of 60º in steel, which corresponds to 56.8º in aluminum. The probe was coupled to the plate using Sonotech Pyrogel ultrasonic couplant and was secured in place with adhesive mounts and plastic ties. The resulting wavefield was imaged using a custom XY scanner and Polytec OFV-551 fiber vibrometer and Polytec OFV-5000 fiber vibrometer controller over a 30 mm × 30 mm area, with a 0.25 mm step size in both directions, centered at a location

32.5 mm from the transducer. The output of the fiber vibrometer was passed through a 1-10 MHz bandpass filter and digitized by a Cleverscope CS328A oscilloscope at a sampling frequency of 100 MHz. The wavefield data were deconvolved to obtain the equivalent response for a 5-MHz, 2-cycle, Hann windowed, tone burst excitation [39].

3.2 Summary of Experiments

Experiments were performed to evaluate scattered energy from a through-hole as a function of the through-hole fill condition. A summary of the acquired wavefield data is given in Table 3.1.

Table 3.1. Summary of experimental wavefield measurements.

Scan #	Hole Diameter (mm)	Fill Condition
1	No Hole	N/A
2	6.36	Air
3	6.36	Epoxy
4	6.36	Aluminum, Epoxy Coupling
5	6.36	Aluminum, Oil Coupling
6	6.36	Steel, Epoxy Coupling
7	6.36	Steel, Oil Coupling
8	6.36	Half-Steel, Oil Coupling

Before drilling holes, the angle-beam probe was secured to the plate and kept in place for each experiment to ensure that the incident wavefield would remain essentially unchanged between experiments. The scanned area was the same except for any small spatial misalignment that may have occurred between experiments because the plate was removed from the scanner mount to drill a hole or introduce a particular fill condition.

Wavefield data were measured for the undamaged plate, and a drill press and standard drill bit were used to drill a single through-hole with a 6.35 mm diameter drill bit and reamed to 6.36 mm to allow clearance for 6.35 mm metal dowel pins. Wavefield data were collected for the 6.36 mm, air-filled hole. For the next scan, the hole was filled with Loctite E-05CL epoxy adhesive, which was also used to couple the metal inserts to the plate in subsequent scans. In the following scan, a 25.4 mm long, 6.35 mm diameter aluminum dowel pin was inserted and secured into the through-hole such that the length of the dowel extended beyond the faces of both sides of the plate; epoxy was used for coupling. Another aluminum dowel was inserted into the through-hole and coupled using Bel-Ray Food Grade Oil 100 in the fifth scan. In the following two scans, steel dowel pins were inserted into the through-hole and coupled with epoxy and oil, respectively. A final set of wavefield data was obtained after inserting a steel dowel, cut in half lengthwise, into the hole. The half-insert was coupled with oil and positioned such that the steel insert filled the right half of the hole and the left half was air-filled.

3.3 Experimental Wavefield Measurements

The wedge used in this research is designed with a refracted angle that is greater than the first critical angle, and thus should only generate shear waves in the plate, but previous studies have shown that a strong Rayleigh wave is also generated [40]. Therefore the incident wavefield consists of both Rayleigh waves, which propagate along the surface of the plate, and shear waves, which reflect between the two surfaces of the plate in a series of skips. The method described previously for acquiring wavefield data only allows for measurement on the plate's surface. Therefore, it is only possible to measure the out-of-plane motion of elastic waves propagating in the plane defined by the

surface of the plate. Figure 3.1 shows a series of annotated wavefield snapshots for an air-filled, 6.36 mm diameter through-hole, showing the interaction of incident Rayleigh and shear waves with the hole and the resulting Rayleigh, shear, and longitudinal wave scattering.

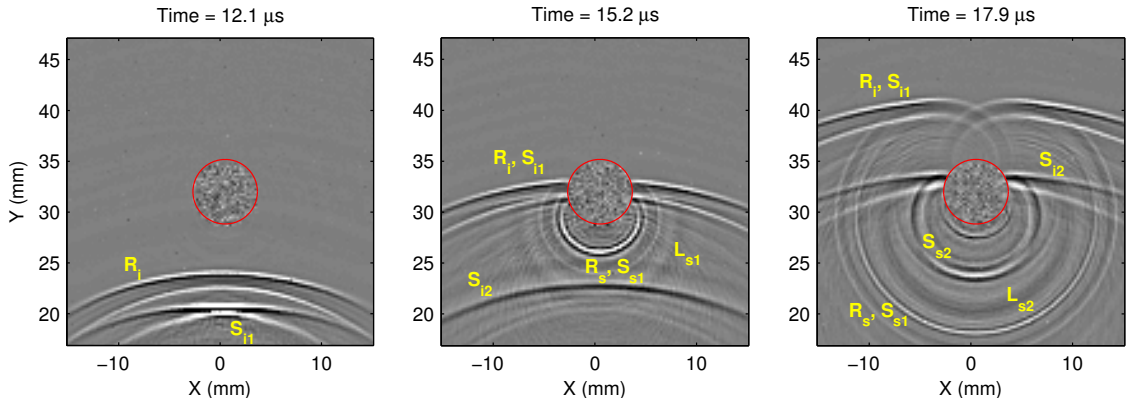

(a) (b) (c)

Figure 3.1. Annotated wavefield snapshots from imaging of an air-filled, 6.36 mm through-hole at (a) 12.1 µs, (b) 15.2 µs, and (c) 17.9 µs. Annotations indicate the wave mode (R-Rayleigh, S-shear, L-longitudinal), the first subscript indicates incident (i) or scattered (s), and the second subscript indicates the skip number.

The snapshots give an indication of the complicated nature of the wavefield data, which results from the multiple shear wave skips; the distance used here of 32.5 mm corresponds to 1.5 skips. Figure 3.1(a) captures two incident waves at 12.1 µs, where the leading wavefront, R_i, is a Rayleigh wave and the second, S_{i1}, is the shear wave from the first skip. At 15.2 µs, shown in Figure 3.1(b), the two incident wavefronts, with differing phase velocities, are incident on the through-hole, resulting in scattered Rayleigh and shear waves, denoted as R_s and S_{s1}. Additionally, incident shear waves interact with the through-hole and are converted to longitudinal waves propagating radially outward from the scatterer. One such longitudinal wave, L_{s1}, is visible in Figure 3.1(b). Figure 3.1(c)

shows the behavior of the incident wavefronts above the through-hole, where waves diffract around the hole. In addition, the snapshot shows a second shear wave, S_{i2}, incident on the through-hole, resulting in a scattered shear wave, S_{s2}, and mode converted longitudinal wave, L_{s2}.

Figure 3.2 shows snapshots of the wavefields for the various fill conditions listed in Table 3.1 at 17.9 μs. The figure illustrates how visual inspection of wavefield data can be useful to gain at least a qualitative understanding of wave scattering. In each case, the shape of the incident and scattered wavefields appear to be very similar; the locations of the waves in each snapshot generally agree. However, the amplitudes of the scattered waves vary non-trivially with the most apparent differences occurring for waves scattering back from the through-hole. The wave behavior within the hole, whose boundary is specified by a red circle, also varies as a function of fill condition. As expected, the area within the hole appears noisy for the air and epoxy fill conditions, but waves are visible within the metal inserts. Since the geometry of the through-hole itself does not change between successive scans, the main differences between wavefields are variations in amplitude, which are not easily quantifiable by eye. Therefore, analysis techniques must be developed that can both distinguish incident and scattered waves and quantify scattering differences.

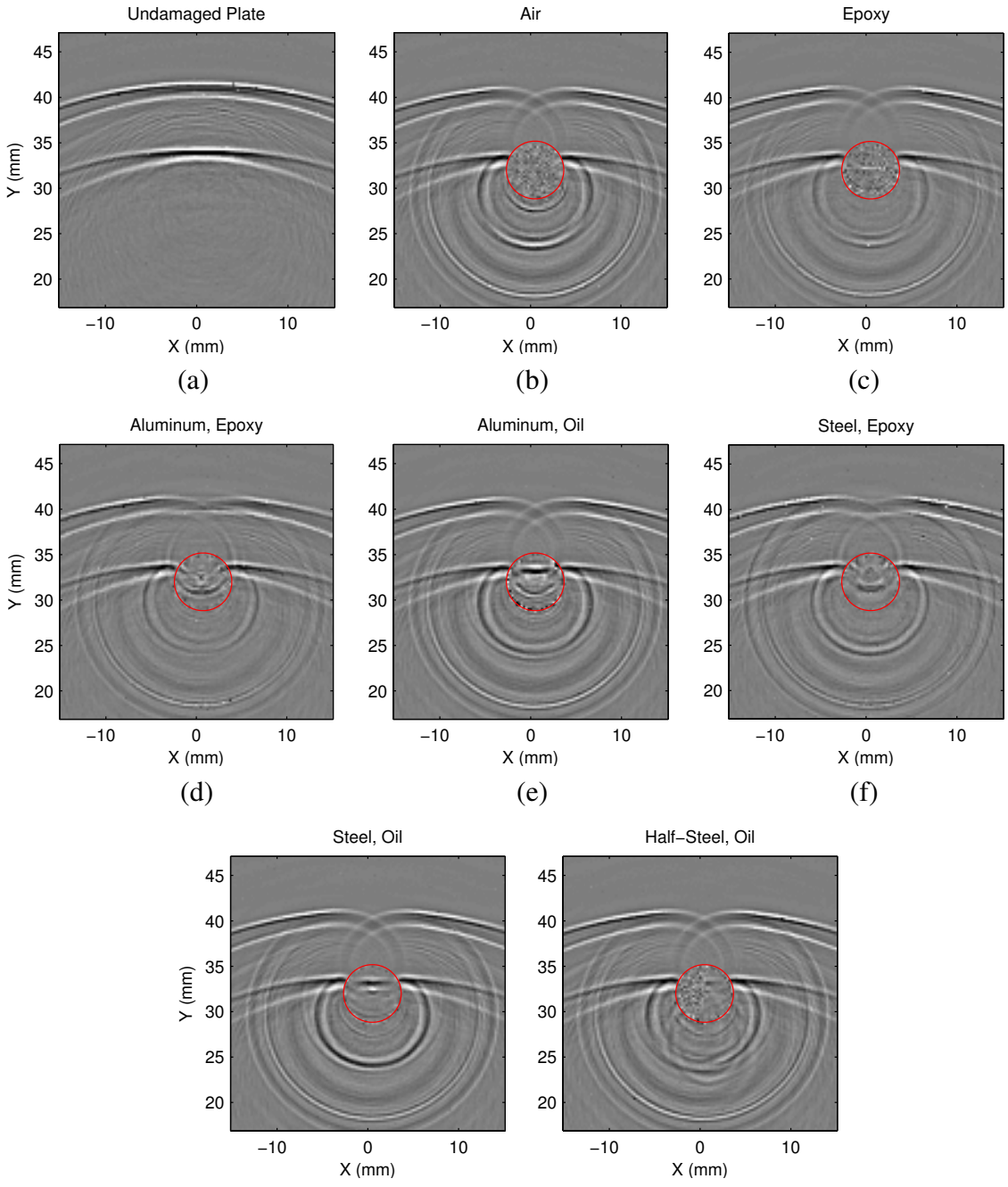

Figure 3.2. Wavefield snapshots at 17.9 µs from imaging of (a) the undamaged plate and through-holes with (b) air, (c) epoxy, (d) aluminum with epoxy coupling, (e) aluminum with oil coupling, (f) steel with epoxy coupling, (g) steel with oil coupling, and (h) half-steel with oil coupling fill conditions.

CHAPTER 4

RADIAL ENERGY MAPPING

In this chapter, the first analysis technique developed to quantify ultrasonic scattering is described. Radial energy maps use experimental wavefield data to obtain scattering as a function of polar angle and phase velocity. Wavefield data from a 6.35 mm thick aluminum plate with a 6.36 mm through-hole is used to show the proposed method for obtaining radial energy maps. A discussion of the noteworthy features of a typical radial energy map is included to provide a basis for interpreting and comparing radial energy maps for the various fill conditions studied in this thesis. Baseline subtraction, which is used to reduce the effects of incident waves and isolate the effects of a defect, is described as a means to enhance the information gained from the method. Scattering patterns are obtained directly from radial energy maps and are used to estimate scattering of each wave mode present in the wavefield. Finally, results are provided for a variety of fill conditions.

4.1 Radial Energy Map Methodology

Application of the radial energy map methodology, shown in Figure 4.1 at various points in the processing chain, results in an energy map showing the energy of scattered waves propagating outward from the defect as a function of angle and phase velocity. The resulting radial energy maps are then used to generate separate angle-beam scattering patterns for Rayleigh, shear, and longitudinal wave modes.

First, the wavefield data are acquired and spatial filtering is performed to remove the noise in the through-hole region. As was done by Dawson [40], a sixth order circular

Butterworth window, $w(x,y)$, is applied where r_c = 4 mm is the radial cutoff and n = 6 is the window order,

$$w(x, y) = \frac{1}{\sqrt{1+\left(r_c / \sqrt{x^2 + y^2}\right)^{2n}}}. \tag{4.1}$$

Spatially windowing the through-hole region improves both the visual presentation of the wavefield data and reduces undesirable edge effects resulting from the sharp transition between signal and noise when utilizing frequency-wavenumber analysis methods.

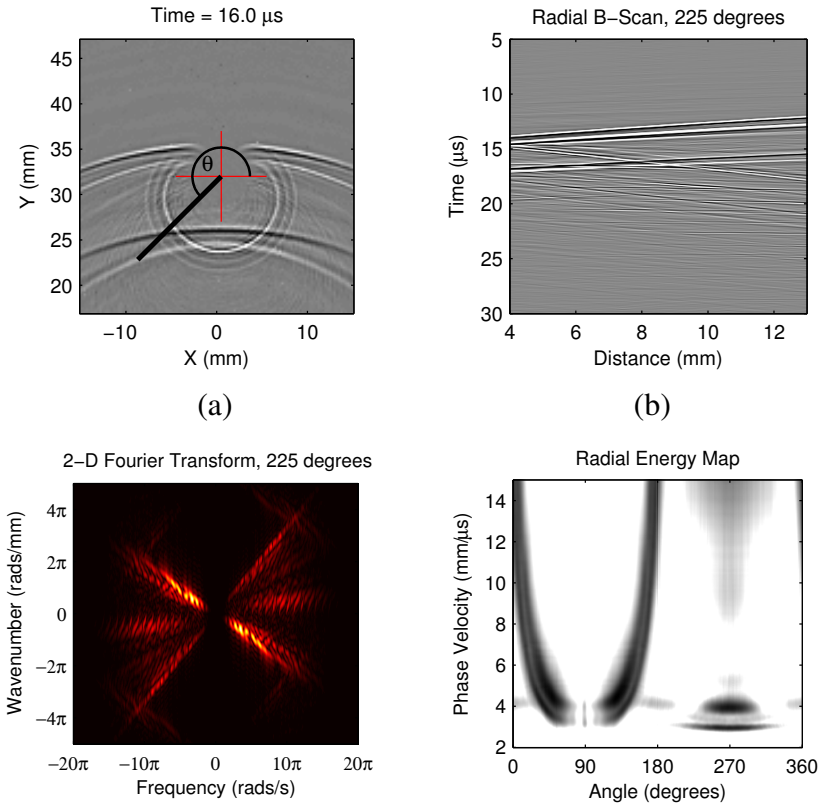

Figure 4.1. Processing steps for generating radial energy maps. (a) Wavefield snapshot showing a radial B-scan line at θ = 225° relative to the center of the hole. (b) Radial B-scan at θ = 225°. (c) Frequency-wavenumber plot of the radial B-scan. (d) Radial energy map formed by accumulating energy along lines of constant phase velocity in the frequency-wavenumber domain for all θ.

Radial B-scan data are found as a function of the polar angle, θ, by interpolating the full wavefield data radially outward from the center of the through-hole along a line defined by θ, starting at a radius of 4 mm, and ending at a radius of 13 mm. Each radial B-scan begins outside the boundary of the hole and remains within the scanned area for all angles. The line in Figure 4.1(a) shows the points used to find the radial B-scan for $\theta = 225°$ overlaid on the wavefield at a single time snapshot. The resulting radial B-scan is shown in Figure 4.1(b), where zero distance refers to the center of the hole and distance increases radially outward.

Radial B-scan data are transformed to the frequency-wavenumber domain via the 2-D FFT; the Fourier transform of the 225° radial B-scan is shown in Figure 4.1(c). In the frequency-wavenumber domain, lines of constant slope are inversely proportional to the phase velocity of waves in the radial B-scan, as described by Eq. (2.7), allowing the energy contribution for a specific phase velocity to be calculated by summing the energy along lines of constant velocity. Since the scattered energy of waves is of interest, only the energy propagating outwards from the origin of the radial B-scan; i.e., with positive velocity, is calculated. Figure 4.1(d) shows the complete radial energy map on a logarithmic scale, which is found by calculating the energy over a range of wave velocities for all radial B-scan angles.

Wavefield imaging of angle-beam bulk waves is complicated by the nature of bulk wave propagation. Unlike guided waves, which propagate through the thickness of the plate, bulk waves propagate within the medium and reflect between the surfaces of the plate. Since wavefield measurements are performed on the surface, the phase

velocity, c_p, is a function of the bulk wave velocity, c, and the angle of wave propagation with respect to the surface normal; i.e., the refracted angle, θ_r:

$$c_p = \frac{c}{\sin\theta_r}. \tag{4.2}$$

As a result, there is a potential ambiguity between the velocity of shear waves propagating at small refracted angles and longitudinal waves propagating at large refracted angles. Energy is assigned to modes as per the phase velocities, but this ambiguity must be considered when interpreting results.

The procedure outlined for computing the radial energy for a particular angle and phase velocity is straightforward when the direction of wave propagation is the same as the direction of the radial B-scan. However, the phase velocity of a wave found from a radial B-scan is difficult to interpret when the direction of wave propagation differs significantly from the radial B-scan direction. In the case of an incident plane wave, the radial phase velocity of a wave, c_r, is a function of the phase velocity on the surface of the plate, given in Eq. (4.2) as c_p, and the difference in angle between propagation direction and radial B-scan direction, θ_d:

$$c_r = \frac{c_p}{\cos\theta_d} \tag{4.3}$$

As expected, a plane wave intersecting broadside to the radial B-scan, with θ_d equal to 90°, would appear to have infinite phase velocity. This phase velocity issue is further complicated because the incident waves are not plane waves, but have a cylindrical wavefront on the surface of the plate.

4.1.1 Interpretation of Radial Energy Maps

Radial energy maps provide a great deal of information about the interaction of incident waves with the through-hole. The following discussion refers to the annotations provided in Figure 4.2, which shows the radial energy map of the air-filled through hole normalized by the maximum radial energy and shown on a logarithmic scale. For radial B-scan angles above the hole; i.e., θ between 0° and 180°, incident Rayleigh and shear waves, shown at **A**, contribute to the calculation of radial energy. The wave velocity and predicted phase velocities observed on the surface of the plate for incident waves are provided in Table 4.1.

Table 4.1. Phase velocities of incident waves on the surface of the plate.

Wave Mode	Nominal Wave Velocity (mm/μs)	Nominal Phase Velocity on Surface (mm/μs)
Rayleigh	2.90	2.90
Shear	3.11	3.72

Since Rayleigh waves propagate on the surface of the plate, the observed phase velocity is equal to the wave velocity. However, the observed phase velocity for shear waves is calculated using Eq. (4.2) for shear waves propagating at a nominal refracted angle of $\theta_r = 56.8$. The asymptotic behavior of incident waves in the radial energy domain is related to the difference in angle between the radial B-scan direction and the direction of propagation of the incident waves, given by Eq. (4.3). As the angle difference increases, the waves pass through the path of the B-scan more quickly and thus have an increasingly large apparent phase velocity. When the radial B-scan direction approaches 0° or 180°, θ_d approaches 90° and the phase velocity approaches infinity.

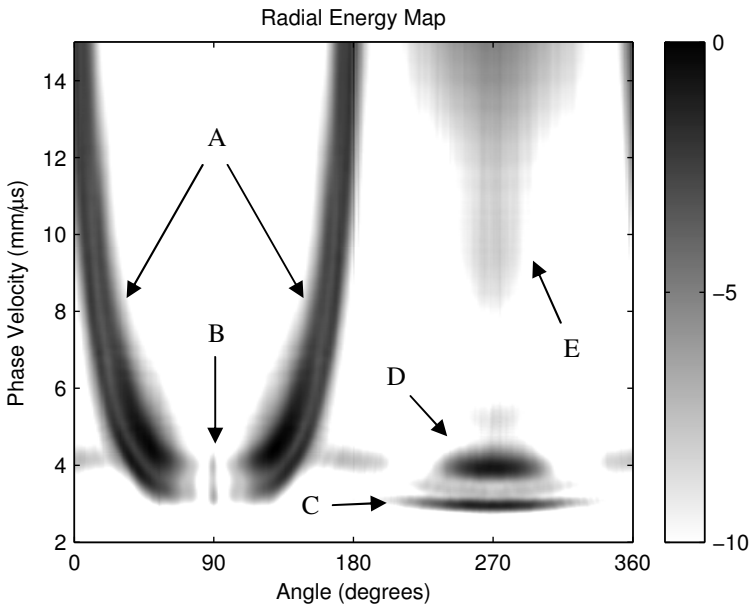

Figure 4.2. Radial energy map for the air-filled 6.36 mm diameter through-hole normalized by the maximum radial energy and shown on a logarithmic scale. Annotations are provided to highlight important features of the radial energy map.

The shadowing effect of the hole is evident at **B**, where incident waves are primarily blocked from radial B-scans centered at 90°. However, viewing wavefield data in the time domain reveals that some incident wave energy diffracts around the hole and constructively interferes above the hole, resulting in a small local maximum at 90°. Similarly, ambiguity issues arise when utilizing radial B-scans for waves above the hole because the diffracted waves do not propagate radially outward from the scatterer, making them difficult to characterize with this method.

In contrast, the incident waves do not contribute to radial energy between 180° and 360° because radial energy is only calculated for waves with positive velocities; i.e., waves that propagate outward from the through-hole. For radial B-scan angles below the hole, incident waves have a negative velocity relative to the radial B-scan direction and are thus not considered. The scattering effect of the hole is best seen by examining

backscattered energy in this region. The scattered energy from Rayleigh, shear, and longitudinal waves, shown in Figure 4.2 at **C**, **D**, and **E**, respectively, is centered at 270° and is spread across a range of polar angles. Rayleigh wave scattering is confined to a small range of velocities since Rayleigh waves propagate along the surface and do not experience the velocity ambiguity phenomenon described by Eq. (4.2). However, the signatures due to scattered shear and longitudinal waves are spread over a range of phase velocities because both propagate within the plate, as discussed previously. For a set range of propagation angles within the plate, Eq. (4.2) shows that longitudinal waves, which have a higher velocity than shear waves, experience more phase velocity spreading in the radial energy domain.

4.1.2 Baseline Subtraction

The effects of a scatterer can be isolated by subtracting two radial energy maps. The goal of baseline subtraction is to remove the effects of incident waves and separate the energy of scattered waves from the energy of the total wavefield. When comparing two scattering scenarios, the radial energy maps can be subtracted point-by-point,

$$E_R(\theta, c_p) = E_C(\theta, c_p) - E_B(\theta, c_p), \tag{4.4}$$

where E_C is the current radial energy map of the wavefield containing the defect or scatterer of interest, E_B is the radial energy map being used as the baseline, generally of the wavefield without the scatterer of interest, and E_R is the residual radial energy map.

Figure 4.3(a) shows an example of baseline subtraction of radial energy maps, where the radial energy from the undamaged plate is subtracted from the radial energy of the 6.36 mm through-hole; the resulting residual is normalized by the maximum radial energy of the baseline and shown on a linear scale. Regions in red correspond to points

where the current radial energy is greater than that of the baseline and regions in blue indicate points where the current radial energy is less than that of the baseline. Baseline subtraction of the radial energy maps has almost completely removed the effects of incident waves from the region above the hole; i.e., for θ between 0° and 180°.

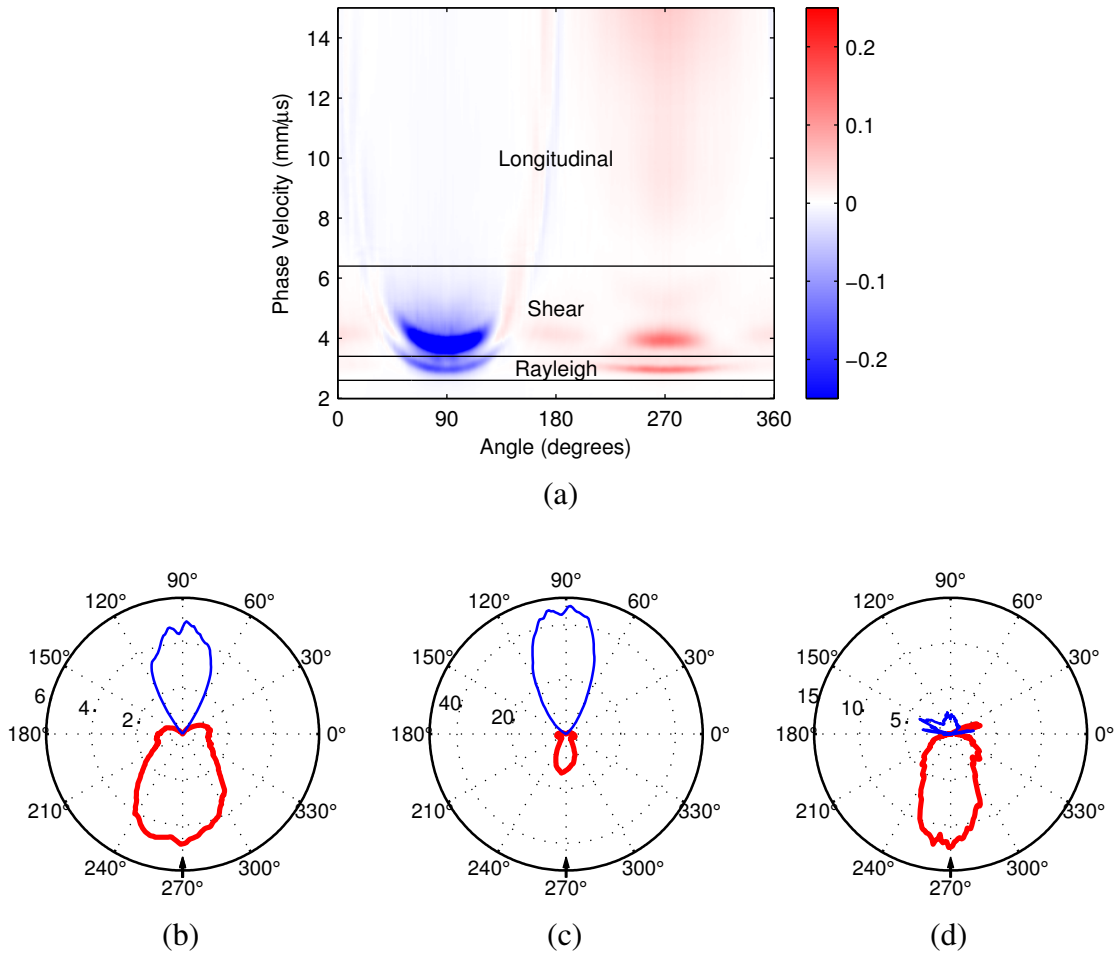

Figure 4.3. Baseline subtraction of radial energy maps acquired before and after drilling the 6.36 mm through-hole. (a) The residual radial energy map is normalized by the maximum radial energy of the undamaged plate and is divided into ranges of wave velocities. Calculated scattering patterns for (b) Rayleigh, (c) shear, and (d) longitudinal wave modes, where red and blue indicate positive and negative residual energy, respectively. The arrows indicate the direction of the incident waves.

4.1.3 Scattering Patterns

Despite the potential ambiguity between different wave modes caused by the refracted angle, the ability to measure the radial energy as a function of the phase velocity is a powerful means to separate and study the scattering of different wave modes, especially for wave velocities where this ambiguity does not exist. Scattering patterns for the three wave modes of interest, Rayleigh, shear, and longitudinal, can be generated by summing along the range of phase velocities corresponding to the desired wave mode in the radial energy map,

$$S(\theta) = \sum_{c=c_a}^{c_b} E_R(\theta, c)\,, \tag{4.5}$$

where $S(\theta)$ is the angular scattering pattern, $E_R(\theta, c)$ is the residual radial energy for polar angle θ and phase velocity c and the range of velocities considered for a particular wave mode is restricted by c_a and c_b.

Table 4.2. Phase velocity ranges for generating scattering patterns.

Wave Mode	Nominal Wave Velocity (mm/μs)	Phase Velocity Range (mm/μs)	Refracted Shear Angle (Degrees)	Refracted Longitudinal Angle (Degrees)
Rayleigh	2.90	2.6–3.4	90.0–66.3	—
Shear	3.11	3.4–6.4	66.3–29.1	90.0–80.2
Longitudinal	6.31	6.4–14	29.1–12.8	80.2–26.8

Table 4.2 summarizes the phase velocity ranges used to produce scattering patterns for each wave mode. Since the Rayleigh wave propagates along the surface, its range of phase velocities is much smaller than the range for the shear and longitudinal waves. The upper Rayleigh phase velocity of 3.4 mm/μs overlaps into the range of possible shear wave velocities for shear waves at refracted angles greater than 66.3°. This

value was selected because significant Rayleigh wave energy leaks into this range due to the mismatch in radial B-scan angle and propagation angle as per Eq. (4.3), even after baseline subtraction. Shear waves at large refracted angles, and correspondingly low phase velocities, are unlikely to have substantial energy within the scanned area due to their larger skip distances. Similarly, high phase velocity shear waves with refracted angles less than 29.1° can be confused with longitudinal waves with refracted angles greater than 80.2°. This confusion is unlikely because shear waves with this steep of a propagation angle should have small out-of-plane displacements and thus low recorded amplitudes, and the shallow longitudinal waves should not have much energy within the scanned region. Figure 4.3(a) shows the normalized residual radial energy map separated into bands that illustrate the range of phase velocities listed in Table 4.2, which are used to calculate the scattering pattern of each wave mode.

Energy scattering patterns, shown in Figures 4.3(b), (c), and (d) for the Rayleigh, shear and longitudinal modes, respectively, were calculated using Eq. (4.5) and the wave velocity ranges given in Table 4.2. The direction of arrival of incident waves on the through-hole is indicated by the black arrow in each scattering pattern. The thick, red lines indicate that the scattered energy of the current wavefield is greater than that of the baseline, and the thin, blue lines indicate that the introduction of the scatterer reduces the energy as compared to the baseline. The scattering patterns for the Rayleigh and shear modes, shown in Figures 4.3(b) and (c), confirm the shadowing of the incident Rayleigh and shear waves by the through-hole, resulting in reduced forward scattering and increased backscattering. The longitudinal scattering pattern in Figure 4.3(d) shows longitudinal waves scattering radially outward below the though-hole and is evidence of

mode conversion from incident shear waves to backscattered longitudinal waves; there is very little longitudinal energy propagating in the forward direction.

4.2 Results of Radial Energy Analysis

In this section the methodology for acquiring radial energy maps is applied to investigate scattering from through-holes in plates as a function of fill condition since changing or unknown boundary conditions can have a significant effect on the performance of ultrasonic NDE methods. Analyzing wave scattering from a through-hole as a function of its fill condition can provide quantitative information about the effects of boundary conditions on scattering. Radial energy maps are found as a function of scattered angle and wave velocity for the eight fill conditions listed previously in Table 3.1, using the methods described earlier in this chapter. Figure 4.4 shows these maps on a logarithmic scale; all radial energy maps are normalized by the maximum radial energy of the undamaged plate.

The wavefields are separated into two groups to incrementally test different aspects of the fill conditions within the hole. First, the effects of varying bulk material within the hole is tested by comparing epoxy, aluminum with epoxy coupling, and steel with epoxy coupling fill conditions. Next the effects of coupling and geometry are studied by comparing scattering for the steel with epoxy coupling, steel with oil coupling, and half-steel with oil coupling fill conditions.

4.2.1 Through-Hole Fill Material

The residual radial energy maps shown in Figure 4.5 are the result of the subtraction of radial energy maps for the air-filled hole from radial energy maps for the epoxy, aluminum with epoxy coupling, and steel with epoxy coupling filled holes, and

highlight the effects of scattering and mode conversion as the interface between the plate and the through-hole changes. The residual radial energy maps in Figure 4.5 are normalized by the maximum radial energy of the air-filled through hole.

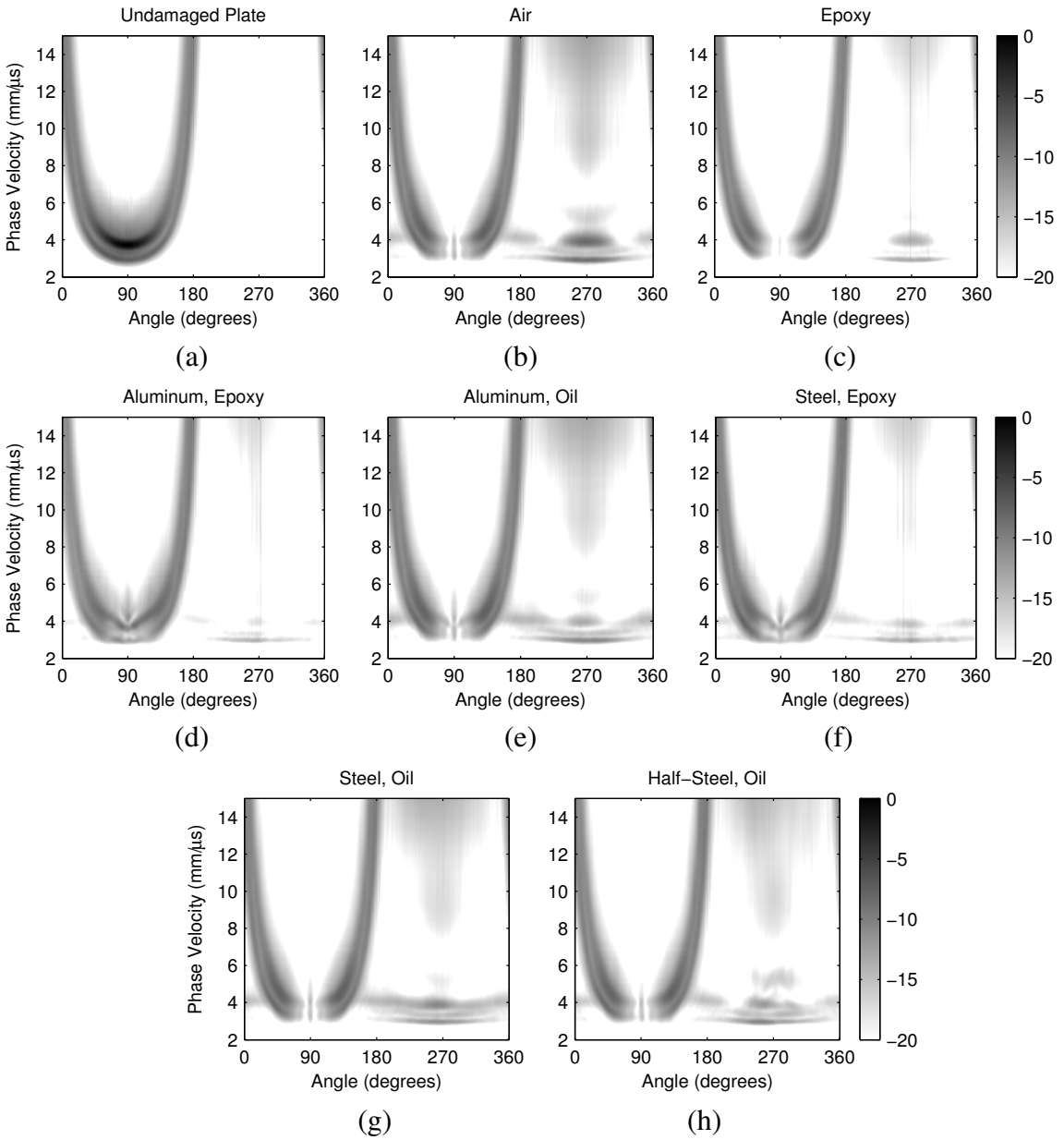

Figure 4.4. Radial energy maps for (a) the undamaged plate, and through-holes with (b) air, (c) epoxy, (d) aluminum with epoxy coupling, (e) aluminum with oil coupling, (f) steel with epoxy coupling, (g) steel with oil coupling, and (h) half-steel with oil coupling fillings. All maps are shown on a logarithmic scale normalized by the maximum radial energy of the undamaged plate.

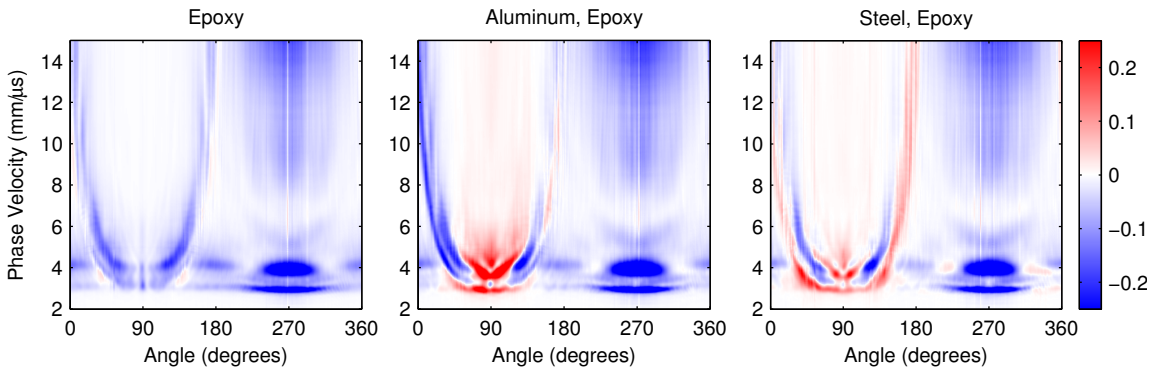

(a) (b) (c)

Figure 4.5. Residual radial energy maps for (a) epoxy, (b) aluminum, and (c) steel inserts in the 6.36 mm through-hole; the air-filled through-hole is the baseline and the metal inserts are coupled with epoxy. Each residual radial energy map is normalized by the maximum radial energy of the air-filled case.

For the epoxy case, radial energy is reduced in all directions and for all wave velocities as compared to the air-filled case. As a result, the residual radial energy map of Figure 4.5(a) is negative for all angles and velocities. Qualitatively, this behavior is expected because energy that was reflected from the air-aluminum interface is coupled into the epoxy and absorbed, reducing the amount of energy that is scattered from the hole. The asymptotic behavior at 0° and 180° in Figure 4.5(a) resembles the radial energy maps found without baseline subtraction, suggesting that subtraction of radial energy maps does not completely remove the incident wave energy. Since the changes in scattering are small as compared to the hole versus no-hole situation, imperfect baseline subtraction becomes more of an issue when comparing scattering of the various fill conditions to that of the air-filled hole.

Similar effects resulting from imperfect baseline subtraction can be seen in Figures 4.5(b) and (c) for the aluminum and steel inserts. The residual radial energy maps for the metal inserts show that scattering and mode conversion between 240° and 300°

are significantly reduced, undoubtedly because energy is coupled into the inserts rather than backscattered. In fact, although not shown here, the wavefield snapshots show waves propagating within the metal inserts and ringing within the boundary of the through-hole, which results in small-amplitude secondary waves propagating outward from the through-hole.

Incremental scattering plots for the Rayleigh, shear, and longitudinal modes are provided in Figure 4.6 for the epoxy, aluminum, and steel through-hole fill conditions as compared to the air-filled hole. Each scattering pattern is passed through a three point averaging filter to remove sharp transitions and allow for better visual comparison. Because scattering patterns are found using residual radial energy data, they quantify the scattering caused by introducing a material into the through-hole as compared to an air-filled hole.

As expected, each of the three fill conditions reduces the backscattered energy for all three modes as compared to the baseline. The aluminum insert causes the greatest reduction in backscattering, which is likely because it is best matched to the plate, in terms of acoustic impedance. In the forward direction, the aluminum with epoxy coupling exhibits the largest increase in forward scattering for Rayleigh and shear modes, which is shown by comparing the positive lobes centered at 90° for Rayleigh and shear scattering patterns from the aluminum insert, shown in Figures 4.6(b) and (e), to those of the steel insert, shown in Figures 4.6(c) and (f); the epoxy fill condition does not promote forward scattering, which is likely because incident energy that is transmitted into the epoxy filling is absorbed, rather than transmitted through the material as is the case for the metal inserts.

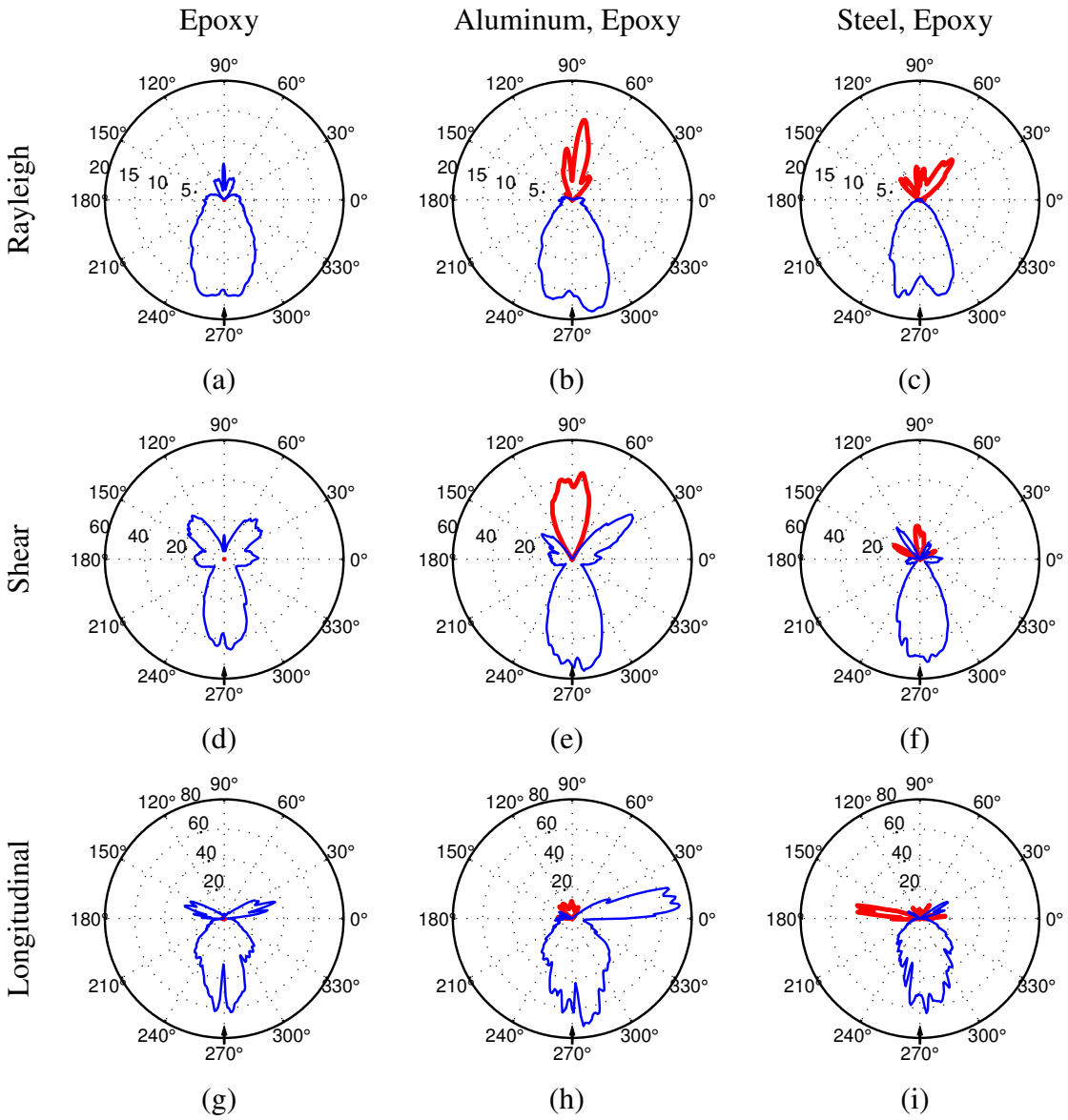

Figure 4.6. Incremental scattering patterns for Rayleigh (a,b,c), shear (d,e,f), and longitudinal (g,h,i) wave modes from epoxy, aluminum, and steel inserts in the 6.36 mm through-hole; the air-filled through-hole is the baseline.

Although the radial energy method is very useful for obtaining scattering patterns from through-holes in plates, the inability to remove the effects of incident waves by baseline subtraction results in artifacts in the scattering patterns. Positive and negative lobes in the scattering patterns for radial B-scan angles from 0 to 70° and 110 to 180° are

likely artifacts of incident energy that remain after baseline subtraction. This behavior is best shown in Figures 4.6(d) and (e), where negative lobes exist at 45° and 135°, and similarly in Figures 4.6(g), (h), and (i), at approximately 15° and 165°.

Ideally, the scattering patterns in Figure 4.6 should be symmetrical because of the geometry of the through-hole. The asymmetry of the various scattering patterns is likely due to error in the alignment of the angle-beam probe with the hole such that incident waves do not propagate directly at the center of the hole.

4.2.2 Coupling and Geometry

In the second set of comparisons, the effects of scattering from a complete and partial steel filled through-hole are investigated for two different coupling scenarios. Residual radial energy maps for the steel with epoxy coupling, steel with oil coupling, and half-steel with oil coupling are shown in Figure 4.7; Note that Figures 4.5(c) and 4.7(a) both show the residual radial energy map for the epoxy coupled steel insert.

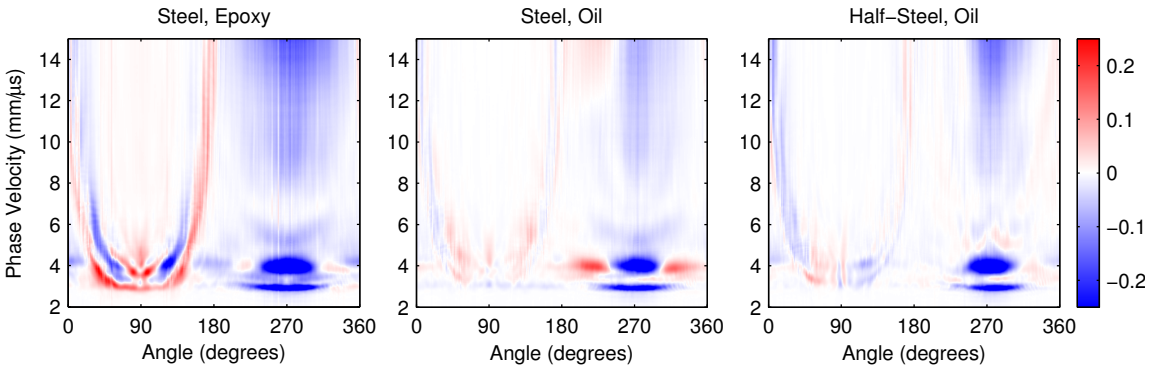

Figure 4.7. Residual radial energy maps for (a) steel with epoxy coupling, (b) steel with oil coupling, and (c) half-steel with oil coupling in the 6.36 mm through-hole; the air-filled through-hole is the baseline. Each residual radial energy map is normalized by the maximum radial energy of the air-filled case.

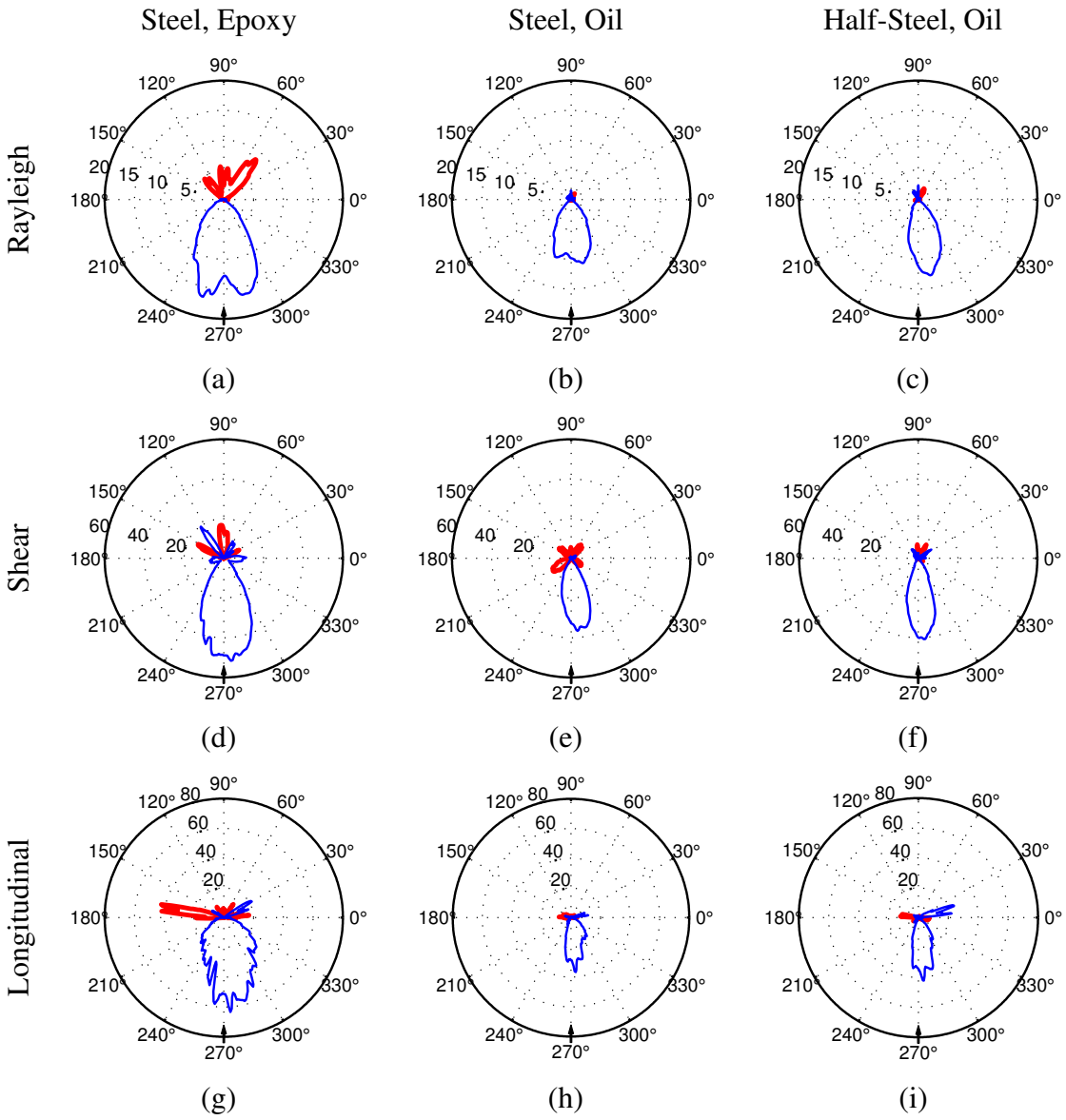

Figure 4.8. Incremental scattering patterns for Rayleigh (a,b,c), shear (d,e,f), and longitudinal (g,h,i) wave modes from steel with epoxy coupling, steel with oil coupling, and half-steel with oil coupling inserts in the 6.36 mm through-hole; the air-filled through-hole is the baseline.

Figure 4.8 shows Rayleigh, shear, and longitudinal scattering patterns for each fill condition, which are obtained from the residual radial energy maps provided in Figure 4.7. As was done for the previous set of fill conditions, each scattering pattern is passed through a three point averaging filter. Note that the scattering patterns in Figures

4.5 and 4.7 utilize the same baseline and normalization factor, and can be directly compared.

As expected, each of the metal inserts reduces the backscattered energy for all three modes as compared to the baseline. Figures 4.8(a) and (b) show Rayleigh scattering patterns for the epoxy and oil coupled steel inserts, respectively, and reveal that epoxy provides better coupling between the aluminum plate and the steel insert as compared to the oil coupling, resulting in increased energy transfer around the insert and reduced backscattering of Rayleigh waves. For the steel and half-steel inserts with oil coupling, in Figures 4.8(b) and (c), the Rayleigh scattering above the hole matches that of the baseline, which indicates that the Rayleigh wave is not transmitted around the insert in either case. As expected, the Rayleigh scattering below the hole for the half-steel insert matches the geometry of the fill condition; the scattering pattern shows a greater difference as compared to the baseline for backscattered angles greater than 270°, which corresponds to the steel-filled side of the through-hole.

Figures 4.8(d), (e), and (f) show shear wave scattering patterns for each fill condition as compared to the baseline. Similar to the Rayleigh scattering patterns, backscattering is reduced for all three fill conditions. At 90°, the steel with epoxy coupling has the largest change in scattering as compared to the baseline, which confirms that the epoxy provides better shear wave transmission than the oil. The asymmetry of the shear scattering for the half-steel insert at angles above the hole provides evidence of the orientation of the insert. Angles less than 90° show an increase in forward scattering, which correspond to radial B-scans on the side of the hole containing the half-steel insert. However, the half-insert only causes a slight asymmetry in the backscattered direction.

Figures 4.7(b) and 4.8(e) show positive residual energy in the steel with oil coupling case for shear velocities centered at 210° and 330°, which may be the result of real scattering or an artifact; additional experimentation is recommended to understand this behavior.

The longitudinal scattering patterns shown in Figures 4.8(g), (h), and (i) exhibit similar characteristics to the shear mode scattering patterns. As expected, longitudinal mode conversion is reduced for all three fill condition and reduced the most for the steel insert with epoxy coupling. However, the half-steel insert does not create asymmetric longitudinal backscattering, as might be expected. Significant longitudinal energy exists for each fill condition around 0° and 180°, which is likely the result of energy feed-through from imperfect baseline subtraction.

CHAPTER 5

DIRECTIONAL ENERGY MAPPING

The second technique presented in this research, directional energy mapping, has also been developed to quantify the scattering of ultrasonic waves from through-holes in plates. Unlike the radial energy mapping method, this method quantifies the energy of scattered waves as a function of propagation direction, rather than along lines extending radially outward from the defect. Because of the circular geometry of the scatterer, the scattering angle is accurately approximated by the propagation direction. The directional energy mapping method is illustrated by applying the technique to wavefield data from a 6.35 mm thick aluminum plate with a 6.36 mm diameter through-hole. Following the progression of Chapter 4 for the radial energy method, scattering patterns are obtained using baseline subtraction for the fill conditions described in Section 3.2.

5.1 Directional Energy Map Methodology

The results at various steps of the directional energy mapping processing chain, which estimate scattering as a function of propagation direction and phase velocity, are provided in Figure 5.1. First, wavefield data are acquired and preprocessed to remove the noise from the hole region using a 6th order circular Butterworth window, given by Eq. (4.1). In addition, a cosine-tapered window, also known as a Tukey window, is applied along the x, y, and t dimensions of the wavefield. A Tukey window, $w(\rho)$, is a one-dimensional window that may be applied along the generic coordinate ρ, and is defined as

$$w(\rho)=\begin{cases}0 & \mathrm{w}<\left|\rho-\rho_0\right| \\ 1 & 0<\left|\rho-\rho_0\right|<\alpha\mathrm{w} \\ 0.5+0.5\cos\left(\pi\frac{\rho-\rho_0-\alpha\mathrm{w}}{2(1-\alpha)\mathrm{w}}\right) & \alpha\mathrm{w}<\left|\rho-\rho_0\right|<\mathrm{w}\end{cases}, \qquad (5.1)$$

where ρ_0 is the center point of the window, 2w denotes the width of the window, and α is the ratio of the length of the taper section to the total window length, which defines the shape of the window. For all wavefields, $\alpha = 0.2$ is chosen for the window in each dimension. For this application, the Tukey window is used to smooth the edges and reduce the noise in the Fourier domain associated with truncation by a rectangular window [11]. Figure 5.1(a) shows a time snapshot following the application of the circular Butterworth and Tukey windows; the smoothing at the edges of the image is evidence of Tukey windowing in the x and y dimensions. Although not evident in Figure 5.1(a), the time range of the Tukey window was chosen from 0 to 30 ms; all wavefield activity is contained within that range.

Following preprocessing, the wavefield, $w(x,y,t)$ is transformed to the Fourier domain via the 3-D FFT to obtain $W(k_x,k_y,\omega)$ where k_x is the x component of the wavenumber, k_y is the y component of the wavenumber, and ω is the angular frequency. Figure 5.1(b) shows a k_x - k_y planar slice of $W(k_x,k_y,\omega)$ at $\omega = 10\pi$ rads/s. The magnitude of the wavenumber, $|k|$, which is related to the angular frequency, ω, and velocity, c, of a propagating wave by Eq. (2.7), is related to the x and y components of the wavenumber by

$$|k| = \sqrt{k_x^{\,2} + k_y^{\,2}}\,. \qquad (5.2)$$

Therefore, for a given frequency, circles of constant radius correspond to constant phase velocity, which allows for mode separation. At 10π rads/s, $|k| = 3.44\pi$ rads/mm for

Rayleigh waves propagating on the surface of the plate, and $|k| = 2.68\ \pi$ rads/mm for shear waves propagating at a nominal refracted angle of $\theta_r = 56.8°$. The magnitude of the wavenumber for longitudinal waves, with phase velocities given in Table 4.2 from 6.4 to 14 mm/μs, ranges from 0.76π to 1.56π rads/mm.

Similarly, the direction of propagation, described by the angle β, of a wave traveling in two-dimensional space is found by

$$\beta = \tan^{-1}\left(\frac{k_y}{k_x}\right), \tag{5.3}$$

where $\beta = 0°$ corresponds to propagation horizontally to the right with β increasing in the counterclockwise direction; forward and backward propagating waves travel at 90° and 270°, respectively.

After transforming the wavefield to the Fourier domain, frequency-wavenumber information for a given propagation direction is found by interpolating the 3-D Fourier domain data along a radial wavenumber, k_r, in the k_x - k_y plane, starting from the origin and extending radially outward at an angle β, for all positive frequencies; the magnitude of the wavenumber considered here ranges from 0 to 4π rads/mm. The line in Figure 5.1(b) shows the points used to obtain frequency-wavenumber information for waves propagating at $\beta = 225°$ as a function of the magnitude of the radial wavenumber and frequency.

Figure 5.1(c) shows the resulting interpolation for $\beta = 225°$. By Eq. (2.7), lines of constant slope in the frequency-wavenumber domain correspond to lines of constant velocity. The energy is found as a function of velocity for waves propagating in a particular direction by integrating along lines of constant slope; i.e., velocity. The

procedure is repeated for all β to obtain the directional energy map shown in Figure 5.1(d) normalized by the maximum energy of the map, which gives the energy of the wavefield as a function of propagation direction and velocity.

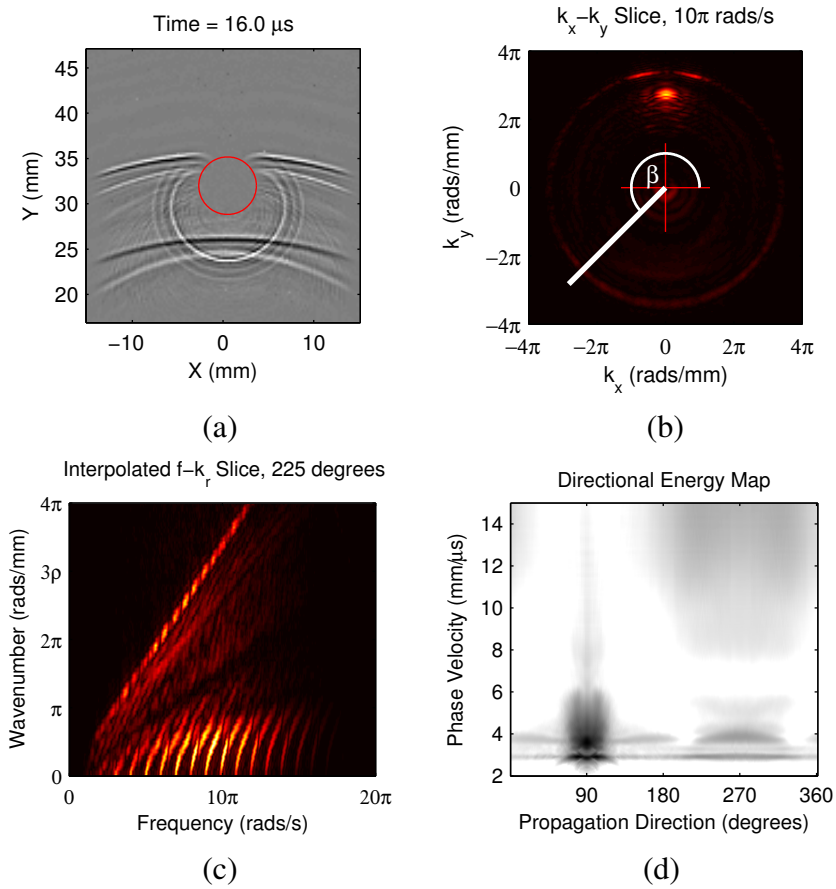

Figure 5.1. Processing steps for generating directional energy maps. (a) The wavefield is preprocessed to remove noise in the hole region and smooth edges. (b) 3-D FFT of wavefield with line along radial wavenumber at β = 225°. (c) Frequency-wavenumber plot of interpolated 3-D FFT for β = 225°. (d) Directional energy map formed by accumulating energy along lines of constant phase velocity in the frequency-wavenumber domain for all β.

As mentioned previously during the development of the radial energy mapping methodology, the measurement method used to acquire wavefields measures out-of-plane motion on the surface of the specimen. Since bulk waves propagate within the plate,

reflecting off of the plate's surfaces, the velocity ambiguity related to the angle of wave propagation with respect to the surface normal described by Eq. (4.2) must be considered.

5.1.1 Interpretation of Directional Energy Maps

Directional energy maps provide useful information about ultrasonic scattering from a defect, particularly for a through-hole. In this case, scattering in a given direction can be well-approximated by the propagation directions of scattered waves because the axisymmetric geometry of the through-hole causes waves to scatter radially outward.

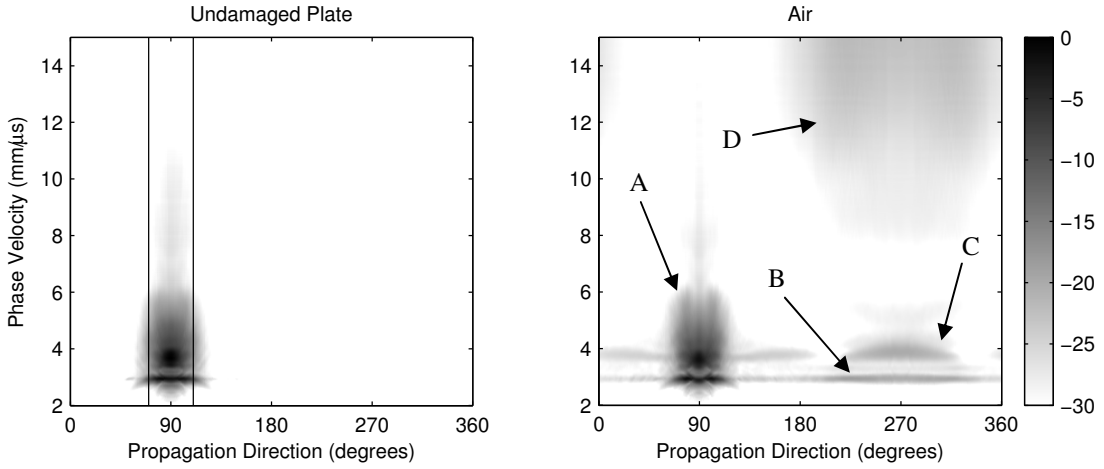

(a) (b)

Figure 5.2. Directional energy maps for the (a) undamaged plate and (b) air-filled 6.36 mm diameter through-hole, with annotations, normalized by the maximum energy of the undamaged plate. Incident directional energy is shown in (a), restricted to angles between 70° and 110°, shown by the black vertical lines.

Figure 5.2 shows directional energy maps for the undamaged plate and the 6.36 mm through-hole on a logarithmic scale normalized by the maximum directional energy of the undamaged plate. Figure 5.2(a), which shows the distribution of directional energy when there is no scatterer, reveals that incident energy is restricted to Rayleigh

and shear modes propagating between approximately 70° and 110°. For the directional energy map with the hole, shown in Figure 5.2(b), the energy of incident waves, shown at **A**, remains restricted in angle and contained at Rayleigh and shear velocities, but the directional energy is reduced because the path of incident waves is disrupted by the hole. Note that energy contributions of waves propagating above the hole are also included in this region, which causes perturbations in the pattern. However, it is difficult to differentiate between incident and scattered waves propagating in the forward direction.

For all other directions, the directional energy mapping technique effectively quantifies scattered energy, as is shown in Figure 5.2(b). Scattering due to Rayleigh waves is shown at **B**. Rayleigh scattering occurs in all directions, with most of the energy propagating near 270°. The energy in the Rayleigh phase velocity band from 0 to 70° and 110 to 180° is the result of Rayleigh wave scattering from the sides of the hole and diffraction around the through-hole. Shear wave scattering, shown at **C**, has very similar scattering characteristics with evidence of both backscattering and diffraction. **D** indicates longitudinal wave scattering, which is present primarily from 180 to 360°, suggesting that mode conversion from incident shear waves to longitudinal waves mostly occurs as a result of reflection at the interface; longitudinal modes do not contribute significantly to the energy of forward propagating waves.

5.1.2 Baseline Subtraction and Scattering Patterns

Directional energy maps can be further exploited by implementing baseline subtraction and obtaining scattering patterns by the same processes as those described in Sections 4.1.2 and 4.1.3 for radial energy maps. Figure 5.3(a) shows an example of baseline subtraction of directional energy maps where the energy from the undamaged

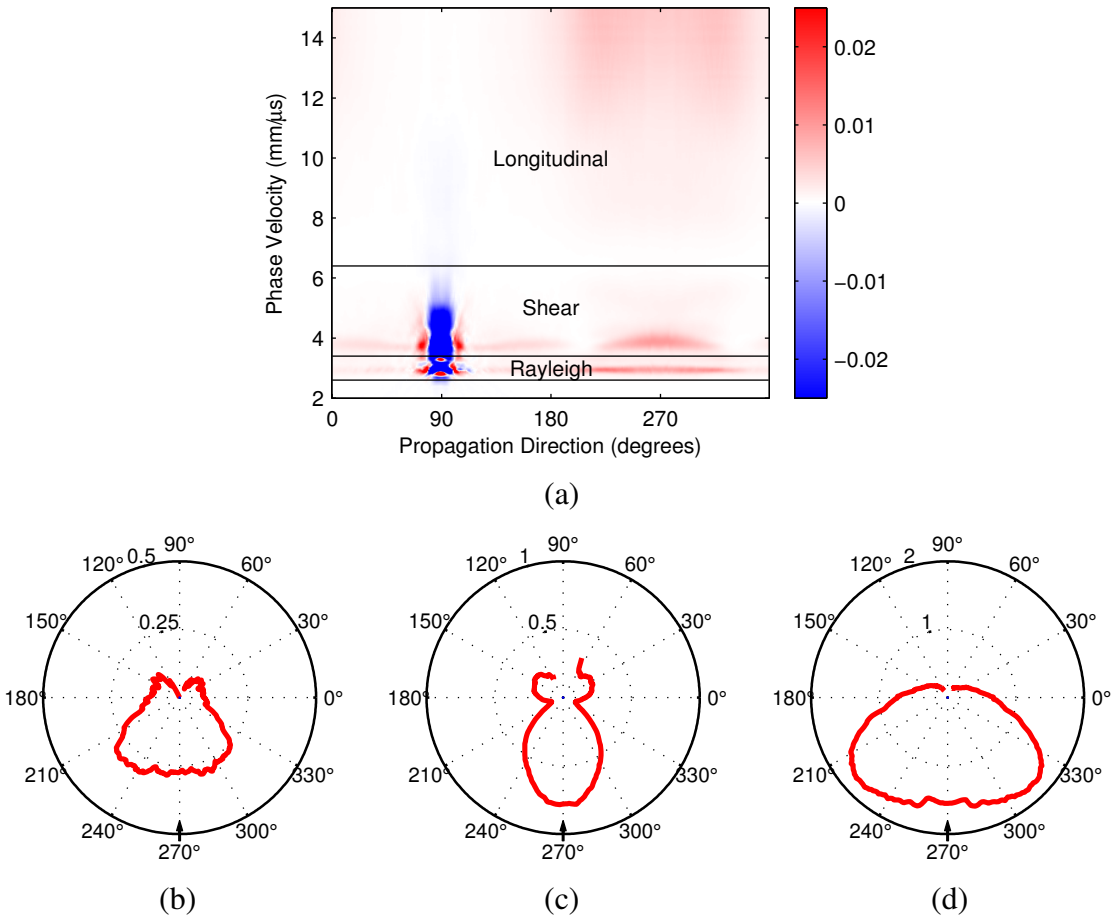

Figure 5.3. Baseline subtraction of directional energy maps acquired before and after drilling the 6.36 mm through-hole. (a) The residual directional energy map is normalized by the maximum directional energy of the undamaged plate and is divided into ranges of wave velocities. Calculated scattering patterns for (b) Rayleigh, (c) shear, and (d) longitudinal wave modes, where red and blue indicate positive and negative residual energy, respectively. The arrows indicate the direction of the incident waves.

plate is subtracted from that of the 6.36 mm through-hole, normalized by the maximum energy of the undamaged plate. As mentioned previously, the introduction of the hole reduces the energy of incident waves as compared to the undamaged plate, which is expected because the hole interrupts the path of incident waves within the wavefield and prevents them from propagating in the upper half of the scan area, resulting in less total energy propagating near 90°. At all other directions and phase velocities, scattering from

the hole causes an increase in residual energy. However, the magnitude of scattered waves is much less than the residual energy of incident waves for the current and baseline directional energy maps chosen here. Since the residual energy of the incident waves is much stronger than that of the scattered waves, a small linear scale is required to view the scattering. As a result, the residual energy at incident wave propagation directions and phase velocities is saturated in the map.

Scattering patterns, shown in Figures 5.3(b), (c), and (d), are obtained directly from the residual directional energy map by application of Eq. (4.5) for the phase velocity ranges given in Table 4.2. Because primary interest is in the scattering from the through-hole and there is a large difference in the magnitude of residual energy at incident and scattered directions, the residual energy at angles corresponding to incident waves; i.e., from 70° to 110°, is excluded from all scattering patterns. For each wave mode, the magnitude of scattering is strongest in the backscattered direction and tapers as the propagation direction approaches 0° and 180°. For the Rayleigh and shear scattering patterns, the lobes at 30° and 150° correspond to energy of incident waves diffracting around the hole, while Figure 5.3(c) reveals that some longitudinal scattering is present in the forward direction.

5.1.3 Spatial Windowing

To this point, the directional energy mapping method has been introduced by operating on the wavefield for the entire scanned area. By nature, the 3-D Fourier transform gives a measure of the contribution of wave modes as a function of propagation direction and velocity; information about the temporal and spatial location of waves is not available in the Fourier domain. As mentioned previously, the directional energy map

method assumes that the direction of propagation matches the angular location of waves scattering radially from the through-hole, which holds true for backscattered waves. However, diffracted waves, which are located in the shadow region above the hole, do not scatter radially outward. Spatial windowing of the full wavefield in the time-space domain can be used to isolate scattering in a localized region within the scanned area and allow for better characterization of scattering, particularly in the shadow region above the hole.

Figure 5.4 illustrates the effects of spatial windowing by showing directional energy maps for the three regions shown in Figure 5.4(a). The 2-D spatial window for each region is created using x and y directional Tukey windows, as described in Section 5.1 and defined by Eq. (5.1). The resulting energy maps for an air-filled hole are shown in Figures 5.4(b), (c), and (d) for the full wavefield, the area below the hole, and the shadow region, respectively. Each energy map is individually normalized by the maximum directional energy of the undamaged plate for their respective windowed regions. Analysis of Figures 5.4(c) and (d) gives information about the spatial location and behavior of waves within specific regions of the scanned area and provides insight into the structure of the full wavefield directional energy map shown in Figure 5.4(b). The energy in the forward direction of Figure 5.4(c) is due entirely to incident waves, which differs from the shadowed region where forward propagating waves are caused by wave diffraction, shown in Figure 5.4(d). These two energy patterns contribute to the shape of forward propagating waves shown in Figure 5.4(b).

As expected, the energy distribution in the backscattered direction is approximately the same in Figures 5.4(b) and (c) for directions between 210° and 330°;

the region below the hole accounts for all waves traveling at 270 ± 60°, and is limited to a 120° width because of the location of the region with respect to the hole. Similarly, the directional energy map for the shadow region only has energy distributed in the forward direction because of its location above the hole. As illustrated in Figure 5.4, spatial windowing of the full wavefield allows for directional energy to be evaluated for specific regions and can be used to further study the effects of fill condition on scattering.

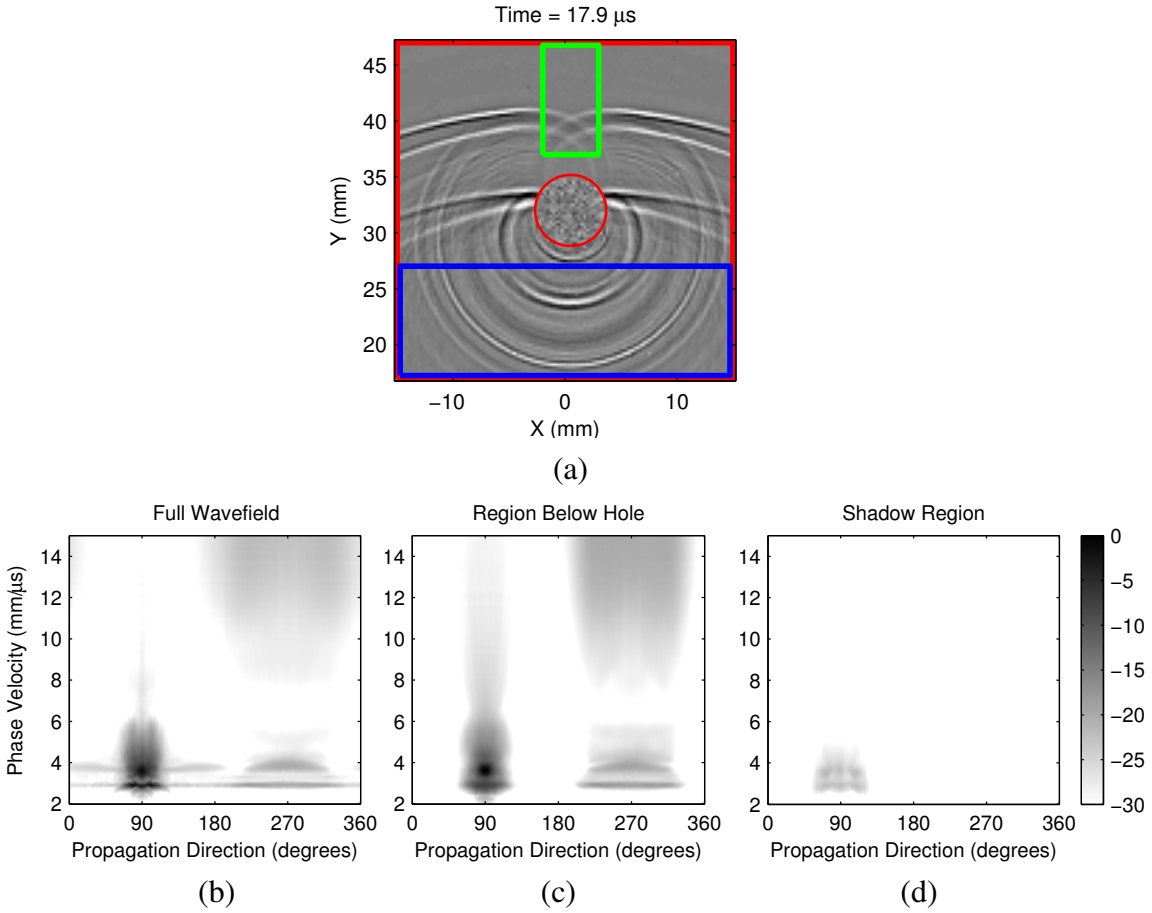

Figure 5.4. Directional energy maps for spatially windowed wavefield of air-filled through-hole. (a) The full wavefield is windowed to find the directional energy for (b) the full wavefield (red), (c) the region below the hole (blue), and (d) the shadow region (green). Each directional energy map is individually normalized by the maximum directional energy of the undamaged plate for each map's respective window.

5.2 Results of Directional Energy Analysis

The directional energy map methodology is used to obtain scattering information from through-holes in plates using the full wavefield for each fill condition. Energy maps are obtained for the various fill conditions summarized in Section 3.2 and Table 3.1 and are shown in Figure 5.5; note that the maps are shown on a logarithmic scale normalized by the maximum directional energy of the undamaged plate. Baseline subtraction in the directional energy domain is used with the air-filled hole as the baseline to estimate changes in ultrasonic scattering for each fill condition as compared to an air-filled hole. Residual directional energy maps are divided into two groups to separately test the effects of the fill material and the coupling/geometry of the filling. Although the results in the following sections allow very similar conclusions about the effects of fill conditions to be drawn as discussed for the radial energy method, directional energy maps and scattering patterns are presented for each fill condition. Presenting results for both methods in the same format allows for direct comparison of the two methods, which is discussed in Chapter 6. Finally, directional energy maps are presented for the shadow region above the hole to demonstrate the usefulness of spatial windowing to supplement scattering analysis through directional energy mapping.

5.2.1 Through-Hole Fill Material

Residual directional energy maps and corresponding scattering patterns for the epoxy, aluminum, and steel fill conditions are shown in Figures 5.6 and 5.7, respectively, normalized by the maximum directional energy of the air-filled hole. Similar to the results presented in Section 4.2.1, the incremental scattering results highlight the changes in ultrasonic scattering as the bulk material within the through-hole changes.

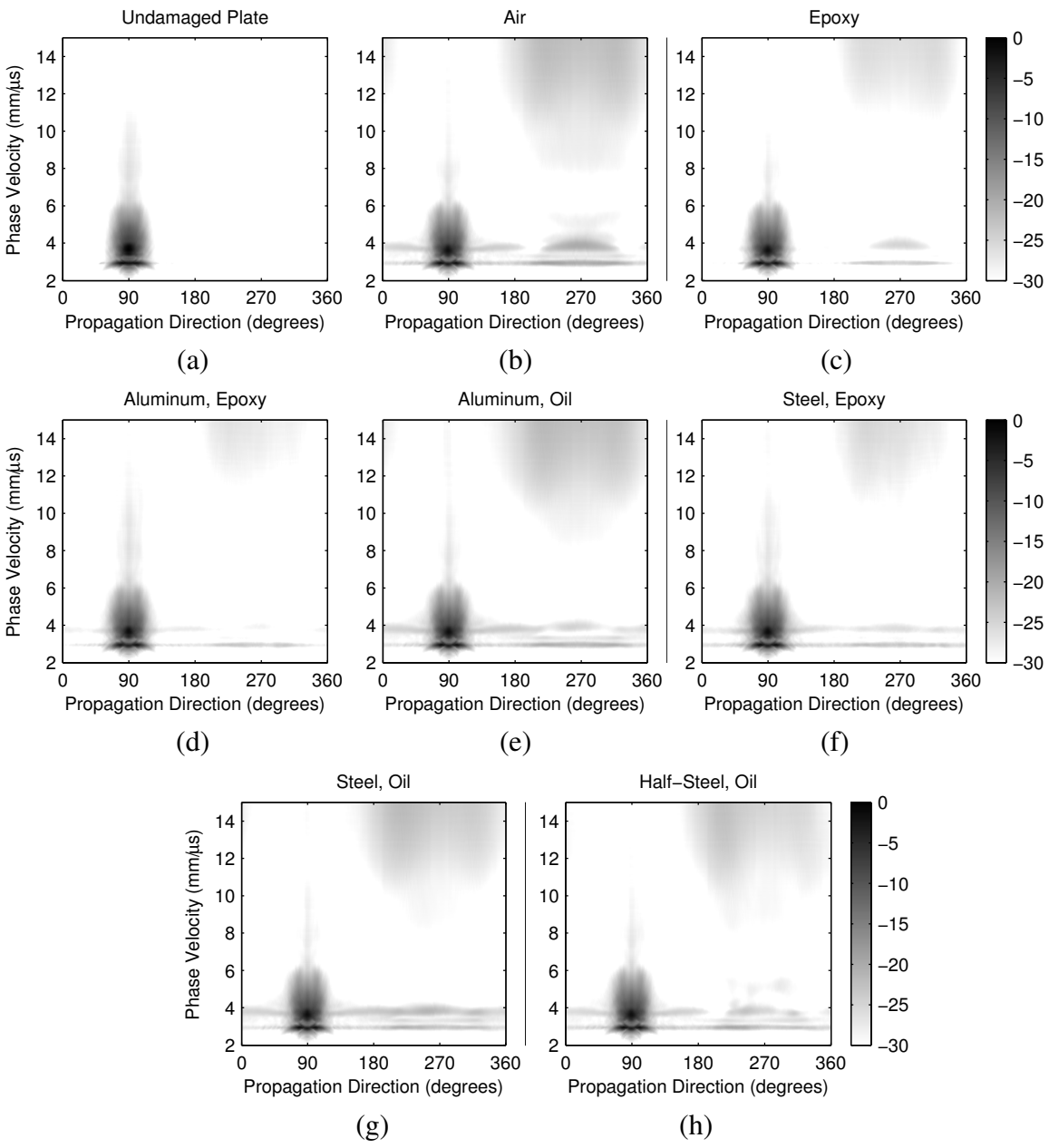

Figure 5.5. Directional energy maps for (a) the undamaged plate, and through-holes filled with (b) air, (c) epoxy, (d) aluminum with epoxy coupling, (e) aluminum with oil coupling, (f) steel with epoxy coupling, (g) steel with oil coupling, and (h) half-steel with oil coupling. All maps are obtained from the full wavefield and shown on a logarithmic scale normalized by the maximum directional energy of the undamaged plate.

For each fill condition, scattering is reduced in approximately all directions and velocities, as shown in Figure 5.6. Energy that was previously reflected from the air-aluminum interface is coupled into the fill material, reducing the amount of backscattering from the hole. Additionally, scattered energy is also reduced in the forward direction from 0 to 70° and 110 to 180° because incident energy is coupled into each material and absorbed or redirected rather than scattered or diffracted around the hole as in the air-filled case.

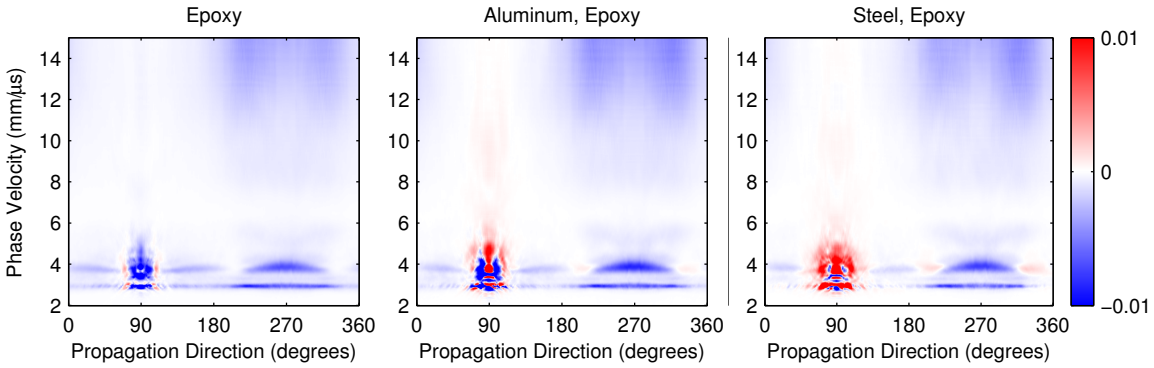

(a) (b) (c)

Figure 5.6. Residual directional energy maps for (a) epoxy, (b) aluminum, and (c) steel inserts in the 6.36 mm through-hole; the air-filled through-hole is the baseline and the metal inserts are coupled with epoxy. Each residual energy map is normalized by the maximum directional energy of the air-filled case.

Although the residual directional energy maps are difficult to interpret around 90°, some information can be obtained about the incident and scattered wavefields above the hole. Most notably, the positive residual energy for the two metal inserts, shown in Figures 5.6(b) and (c) near 90°, suggests that incident energy is transmitted through the inserts and continues to propagate above the hole. Negative residual energy around 90° is more difficult to interpret and may be the result of a real reduction in scattering as

compared to the air-filled hole or from a mismatch in the incident wavefields, which causes poor baseline subtraction. However, since the directional energy of incident waves is generally much greater than that of scattered waves, a relatively small difference in incident energy is likely to have an insignificant effect on the scattered wavefields.

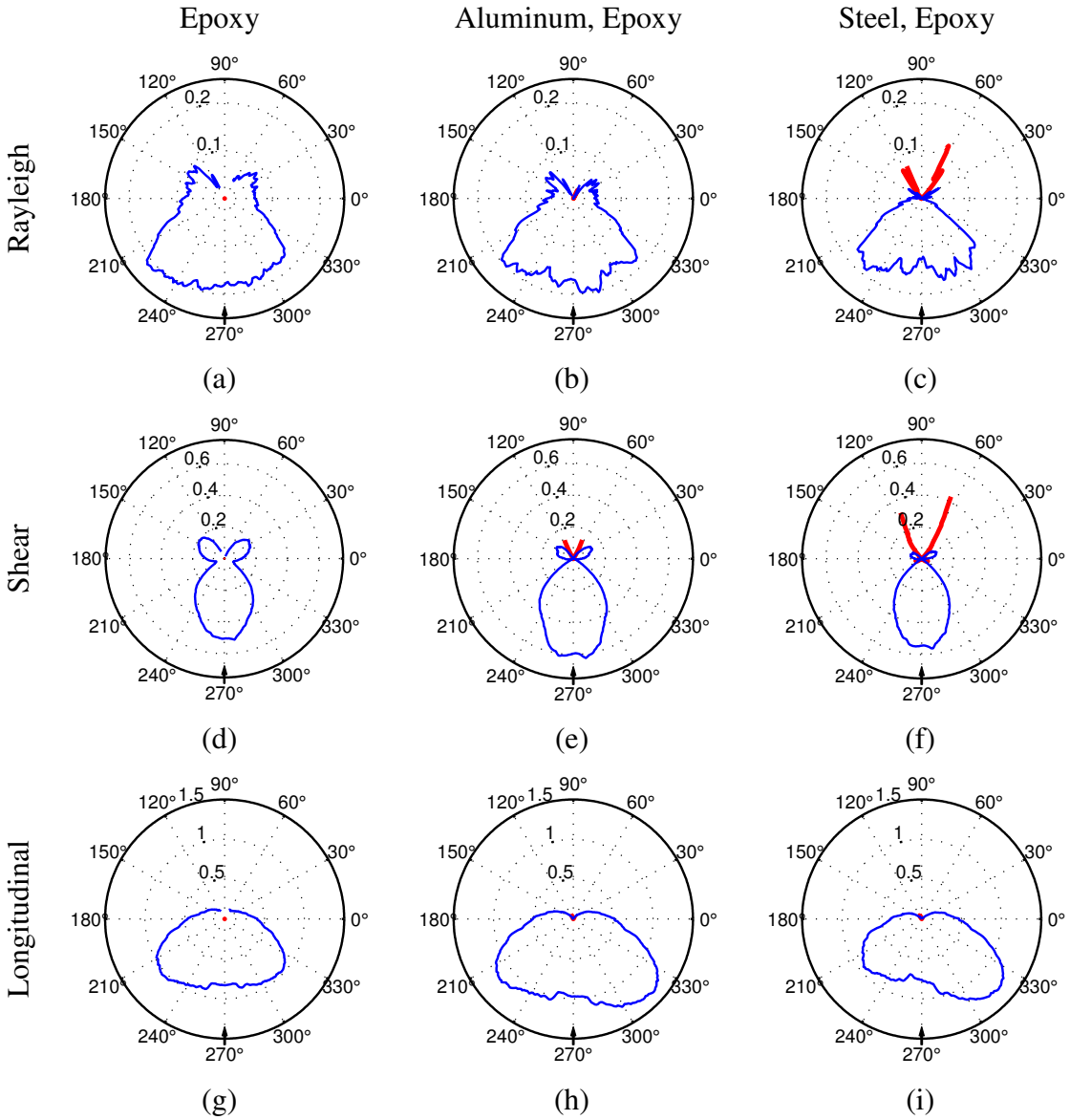

Figure 5.7. Incremental scattering patterns for Rayleigh (a,b,c), shear (d,e,f), and longitudinal (g,h,i) wave modes from epoxy, aluminum, and steel inserts in the 6.36 mm through-hole; the air-filled through-hole is the baseline and angles corresponding to incident waves are excluded from scattering patterns.

Scattering patterns for the Rayleigh, shear, and longitudinal modes are shown in Figure 5.7 for the epoxy, aluminum, and steel fill conditions as compared to the air-filled hole. As mentioned in Section 5.1.2, angles corresponding to the directions of incident waves are excluded from the scattering patterns, but will be addressed in Section 5.2.3. Each fill condition reduces backscattering as compared to the baseline because a portion of incident energy is transmitted into the fill material for each case. Shear and longitudinal scattering is reduced the most for the aluminum insert because it is best matched to the impedance of the plate.

5.2.2 Coupling and Geometry

The effects of coupling and insert geometry on scattering are investigated by comparing directional energy maps for a single fill material for three different situations. Residual directional energy maps for the steel with epoxy coupling, steel with oil coupling, and half-steel with oil coupling are shown in Figure 5.8. The directional energy map for the air-filled wavefield is used as a baseline and all residual directional energy maps are normalized by the maximum energy of the air-filled case. Rayleigh, shear, and longitudinal scattering patterns for each fill condition are provided in Figure 5.9. Results for this section and the previous section are obtained using the same baseline and normalization factor, and results for the steel with epoxy coupling are provided in both sets of figures for ease of comparison.

Comparison of the first two columns of Figure 5.9 provides insight into the effect of coupling on ultrasonic scattering. For Rayleigh, shear, and longitudinal modes, the steel with epoxy coupling reduces the backscattered energy more than the steel with oil coupling. Additionally, the residual directional energy maps, shown in Figure 5.8 for the

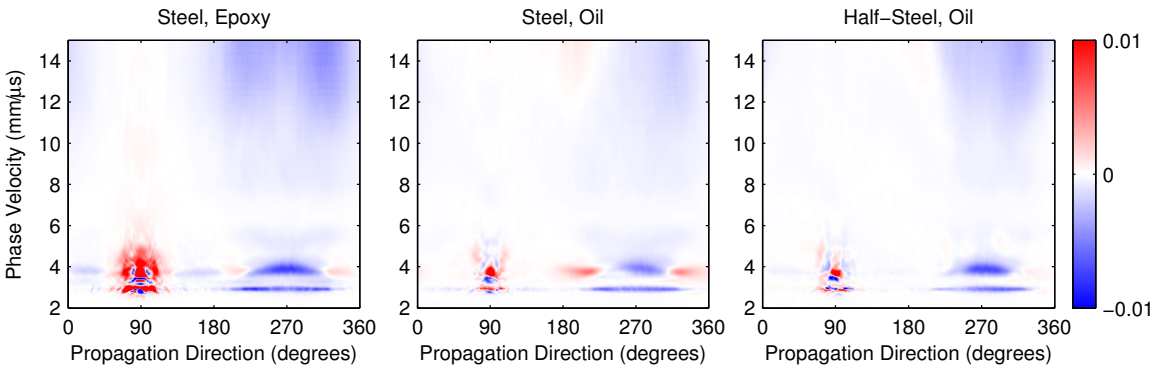

(a) (b) (c)

Figure 5.8. Residual directional energy maps for (a) steel with epoxy coupling, (b) steel with oil coupling, and (c) half-steel with oil coupling in the 6.36 mm through-hole; the air-filled through-hole is the baseline. Each residual energy map is normalized by the maximum directional energy of the air-filled case.

two coupling scenarios, show positive residual energy around 90° for both Rayleigh and shear velocities, which is likely the result of incident wave transmission through the insert. However, the magnitude of the residual energy is greater for the epoxy as compared to the steel, which suggests that epoxy provides better coupling compared to oil for a steel insert in an aluminum plate. Figure 5.9(e) shows positive shear scattering for the steel with oil coupling at approximately 210° and 330°. The reason for these patterns is not understood and additional experiments are recommended to understand this behavior. However, a similar signature is present for the radial energy shear scattering pattern of the steel with oil coupling in Figure 4.8(e), which suggests that the scattering pattern is real, rather than an artifact of either processing method.

Next, the effect of fill geometry is briefly studied by comparing the residual directional energy maps and scattering patterns for steel and half-steel fill condition. For the Rayleigh scattering shown in Figure 5.9(c), the effect of the partial fill condition is apparent; the half-steel insert has a low magnitude of residual energy for angles less than 270°, where the fill condition is similar to that of an air-filled hole, and a large negative

residual energy for angles greater than 270°, where the fill condition resembles a steel insert. However, this asymmetry is not present for shear or longitudinal modes. In fact, for as yet unknown reasons, the scattering patterns for the steel with oil coupling appear more asymmetric for these modes as compared to those of the half-steel case.

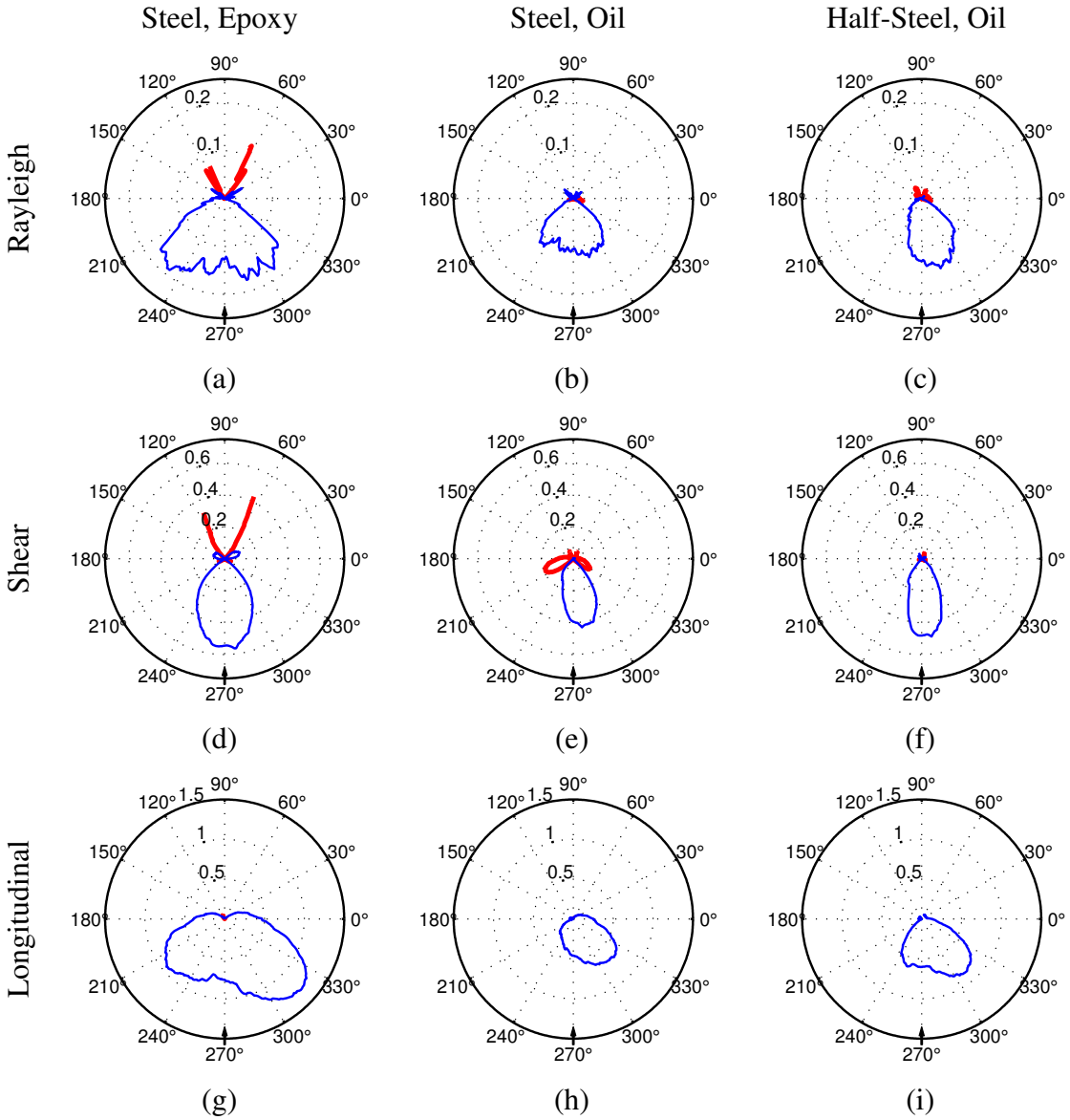

Figure 5.9. Incremental scattering patterns for Rayleigh (a,b,c), shear (d,e,f), and longitudinal (g,h,i) wave modes from steel with epoxy coupling, steel with oil coupling, and half-steel with oil coupling inserts in the 6.36 mm through-hole and angles corresponding to incident waves are excluded from scattering patterns.

5.2.3 Shadow Region

Spatial windowing, as discussed in Section 5.1.3, allows for further characterization of ultrasonic scattering from through-holes in plates. Windowing in the space-time domain is useful for isolating forward scattering for the shadow region above the hole, where incident waves are blocked by the hole. Figures 5.10(a), (b), (c), and (d) show the windowed directional energy maps for through-holes filled with air, epoxy, aluminum with epoxy coupling, and aluminum with oil coupling, respectively; the maps

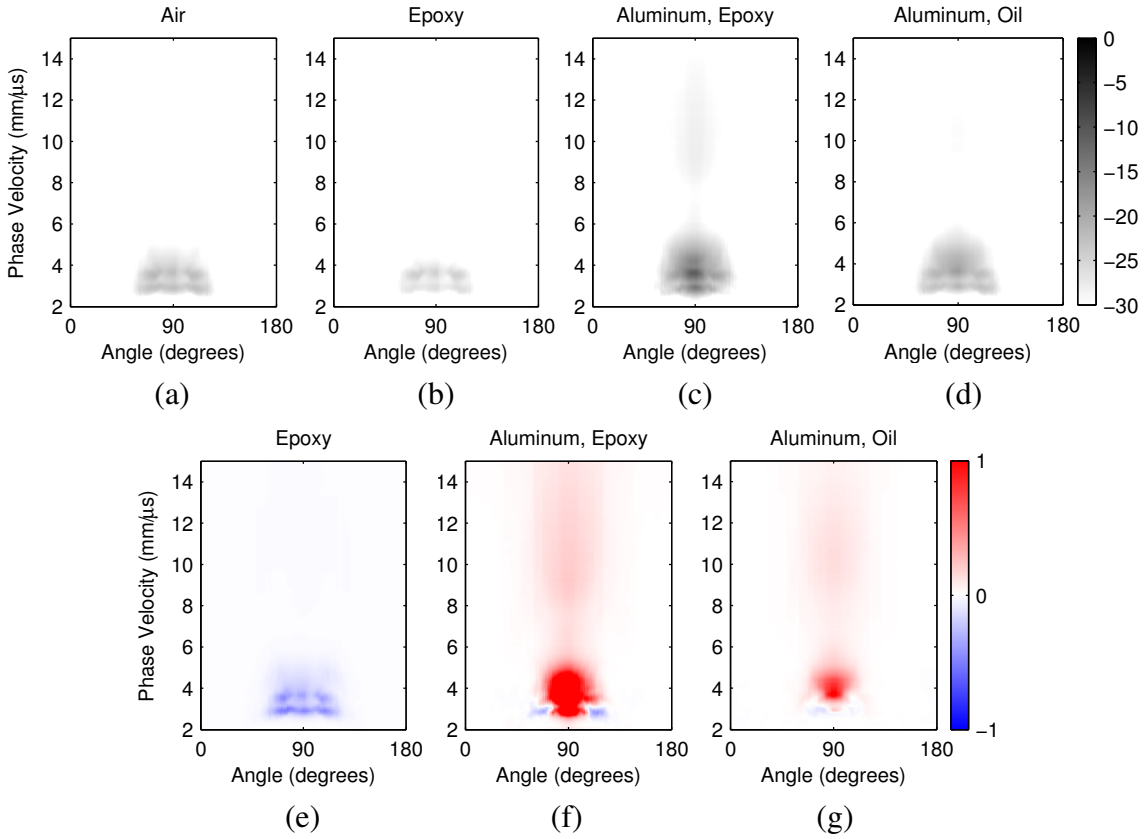

Figure 5.10. Directional energy maps for the shadow region above the hole from (a) air, (b) epoxy, (c) aluminum with epoxy coupling, and (d) aluminum with oil coupling fill conditions, shown on a logarithmic scale. Residual directional energy maps for the shadow region for (e) epoxy, (f) aluminum with epoxy coupling, and (g) aluminum with oil coupling filled holes are shown on a linear scale and found by baseline subtraction with the air-filled hole as the baseline. All maps are normalized by the maximum directional energy of the shadow region for the air-filled case.

are shown on a logarithmic scale, normalized by the maximum windowed directional energy of the air-filled hole. Forward scattering in this region, which is restricted to angles from 60 to 120°, includes diffraction of incident energy around the hole and incident energy that is transmitted through the hole.

Residual directional energy maps are shown in Figures 5.10(e), (f), and (g) on a linear scale, normalized by the maximum energy of the windowed, air-filled hole. As expected, forward scattering above the hole is reduced for the epoxy fill condition as compared to the air-filled hole, as shown in Figure 5.10(e). In addition, Figures 5.10(f) and (g) suggest that forward scattering for both aluminum inserts is due to the transmission of incident waves through the fill material since there is an increase in energy.

Rayleigh, shear, and longitudinal scattering patterns for the epoxy, aluminum with epoxy coupling, and aluminum with oil coupling are shown in Figure 5.11; each scattering pattern is passed through a three point averaging filter for better visual comparison. The shape of each scattering pattern provides evidence about the nature of forward scattering. For example, the Rayleigh scattering for the epoxy fill condition, shown in Figure 5.11(a), is distributed relatively evenly over the full range of angles where forward scattering exists, suggesting that the signature is the result of a change in energy of diffracted waves, which exist for all angles between 60° and 120°. On the other hand, the Rayleigh scattering for the aluminum with epoxy coupling has a large peak at 90°; the narrow distribution suggests that the forward scattering is due to incident Rayleigh waves transmitted through the fill condition or incident shear waves mode converted to Rayleigh waves. However, the pattern also has negative values near 60° and

120°, which is evidence of a reduction of energy of diffracted waves. This behavior is overshadowed by the strong contributions of waves transmitted through the insert. Similarly, the aluminum with oil coupling Rayleigh pattern shows evidence of both diffraction and transmission. The shear scattering patterns for the three fill conditions, shown in Figures 5.11(b), show that both aluminum inserts support the transmission of shear waves through the filled hole, while the epoxy reduces the energy of diffracted waves. Finally, the longitudinal scattering patterns in Figure 5.11(c) show that mode conversion occurs for both aluminum fill conditions, which is likely due to the generation of longitudinal modes as incident waves are transmitted through the fill condition, rather than from diffraction. As expected, the epoxy coupling causes a larger increase in longitudinal forward scattering as compared to the oil coupling.

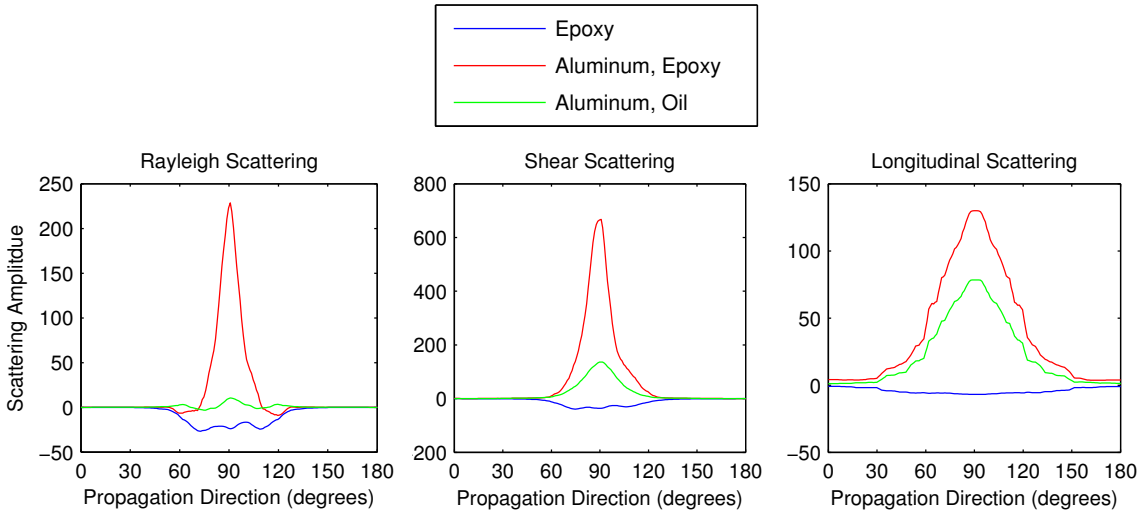

Figure 5.11. (a) Rayleigh, (b) shear, and (c) longitudinal scattering patterns for epoxy (blue), aluminum with epoxy coupling (red), and aluminum with oil coupling (green) filled through-holes. All scattering patterns are obtained from spatial windowing of the shadow region above the hole and passed through a three point averaging filter.

CHAPTER 6

DISCUSSION OF ENERGY MAPPING METHODS

The two signal processing techniques presented in this thesis, radial and directional energy mapping, are both useful for quantifying scattering from experimentally acquired wavefield measurements. Both methods utilize interpolation and multi-dimensional Fourier transforms to extract scattering information; however, the order of processing differs between the methods and significantly alters the nature of the resulting energy maps. This chapter summarizes and compares the radial and directional energy mapping methods in the context of estimating ultrasonic scattering from through-holes in plates and discusses the efficacy of each method.

6.1 Comparison of Methods

The results presented in Sections 4.2 and 5.2 show the expected scattering behavior of through-holes with various fill conditions and demonstrate the effectiveness of the radial and directional energy mapping methods for characterizing ultrasonic wave scattering using wavefield imaging. Characterizing scattering in the form of residual energy maps and scattering patterns allows for the identification of wave modes and independently quantifies the contribution of each mode to wave scattering.

In the radial energy map processing chain, the full wavefield is interpolated along lines extending radially outward from the center of the defect and transformed to the frequency-wavenumber domain via the 2-D FFT, where energy is found as a function of polar angle and phase velocity; except for the issues associated with incident wave propagation direction and radial B-scan direction as described by Eq. (4.3), the scattering

information obtained as a function of angle indicates the actual angular direction of scattered waves. For radial B-scans below the hole, incident waves do not contribute to the radial energy calculation because they have a negative velocity; backscattering waves propagate radially outward from the through-hole and have a positive velocity, which minimizes the wave velocity ambiguity caused by the difference in angle between radial B-scan direction and wave propagation direction.

Characterization of forward scattering utilizing radial B-scans above the hole is more difficult because of the presence of incident waves in radial energy maps and the resulting velocity identification issue that arises when the radial B-scan direction is significantly different from the propagation direction of the incident waves. The simplest method for removing the incident energy is by baseline subtraction of radial energy maps, which significantly reduces the contribution of incident waves but still allows some energy feed-through. In addition, it is difficult to differentiate between residual energy caused by poor baseline subtraction and energy contributions due to actual forward scattering.

In comparison, the directional energy map method utilizes the 3-D FFT to transform the wavefield to the frequency-waveumber domain and then interpolates along a radial wavenumber, which is defined by the propagation direction, before using the same velocity analysis as the radial energy method to obtain energy as a function of propagation direction and phase velocity. As mentioned previously, this method operates under the assumption that scattered waves propagate radially outward from the through-hole, and that their propagation direction corresponds to the angular direction of scattering from the through-hole. Unlike the radial energy method, the angle difference

velocity ambiguity defined by Eq. (4.3) is not relevant to this technique. The directional energy method takes advantage of the fact that incident waves are localized to a relatively limited range of propagation directions and that most of the scattering of interest is in directions that differ from those of incident waves. Although there are issues separating incident and scattered energy for both methods, the directional energy method localizes incident energy more effectively and removes the potential ambiguity that is introduced by using the radial energy method. Incident energy is removed from the directional energy scattering patterns by excluding angles where incident energy is contained. As a result, real forward scattering in this range of angles is also excluded from the scattering patterns.

The effects of incident energy can be mitigated by spatially windowing the full wavefield to obtain directional energy information for a specific region of the scanned area, as was demonstrated in Section 5.2.3. In the shadow region above the hole, incident energy is blocked by the hole and wave propagation is due entirely to forward scattering as a result of diffraction around the hole and transmission of incident energy through the hole. In either case, directional energy mapping coupled with spatial windowing provides a clearer view of scattering above the hole, which cannot be achieved using the radial energy mapping technique. Also, spatial windowing of the area below the hole decouples the energy of incident and forward scattered waves, which allows for direct comparison of incident energy between baseline and current wavefield scans.

6.2 Efficacy of Methods

The effectiveness of each method depends significantly on the geometry of the scatterer. Interpolating radial B-scans from the full wavefield data is a natural choice

because it exploits the cylindrical geometry of the hole and ignores incident energy for radial B-scans in the scattering area below the hole, which is often of primary interest for NDE. Similarly for the directional energy method, the circular nature of the scatterer allows for the assumption that angular scattering can be approximated by the propagation direction of scattered waves. The efficacy of baseline subtraction for both methods also depends on the geometry of the scatterer and is most sensitive to small changes in the scatterer between current and baseline wavefield measurements, such as changes in through-hole fill condition.

Because the methods estimate scattering by different processes, the energy of the scattering patterns for each method cannot be compared directly. Similarly, since scattering patterns for the different wave modes are summed over different ranges of phase velocities, it is difficult to compare the actual energy values between modes, for both methods. However, comparisons of the scattering from the same processing method and mode for different hole scenarios are valid. For example, a comparison of the shear wave scattering patterns from the radial energy method, shown in Figures 4.6(d), (e) and (f) indicates that the reduction in overall backscattering caused by the epoxy, aluminum and steel inserts is similar whereas there is a significant difference in energy in the forward direction. But it is not valid to compare the magnitude of shear scattering to that of longitudinal scattering of the same method; i.e., the patterns in Figures 4.6(g), (h), and (i), or to compare to the magnitude of shear scattering patterns obtained by the directional energy method for the same fill conditions, given in Figures 5.7(d), (e), and (f).

CHAPTER 7

CONCLUSIONS AND RECOMMENDATIONS

7.1 Conclusions

This thesis describes the development and implementation of signal processing techniques to quantify scattering of ultrasonic waves from through-holes in plates using wavefield imaging. Acoustic wavefields were measured and processed to investigate the effects of boundary conditions on ultrasonic scattering. Radial and directional energy maps were presented as methods to estimate scattering of angle-beam shear waves as a function of angle and velocity. The resulting energy maps can be used to estimate the scattering patterns of Rayleigh, shear, and longitudinal modes from a defect or structural feature. The validity of each method was demonstrated in the analysis of a series of experiments considering a through-hole with varying fill conditions. Both of the proposed methods provide useful scattering information and offer metrics for comparing incremental scattering scenarios.

Based on the comparison of the two processing techniques presented in the previous chapter, the directional energy method emerges as a more promising means of estimating scattering from through-holes. Both methods effectively capture the behavior of ultrasonic scattering for the area below the hole and provide very similar information about backscattered energy. In addition, both methods must deal with the interference of incident waves with forward scattering in their respective energy maps, which can be reduced by baseline subtraction. However, the directional energy method is preferred for measuring forward scattering because it avoids the velocity ambiguity introduced by the

radial energy method as a result of the difference in angle between propagating waves and the radial B-scan direction; the directional energy method localizes the energy of incident waves more efficiently. As discussed, the potential application of spatial windowing of the full wavefield before processing by the directional energy method provides another advantage to the directional energy method rather than the radial energy method, primarily for analysis of scattering in the shadow area directly above the through-hole.

Although the methods for generating radial and directional energy maps and scattering patterns presented here are applied to angle-beam wavefield data, the techniques are generally applicable to any 3-D set of wavefield data containing a scatterer of interest. Regardless of the application, the proposed methods for generating scattering patterns from wavefield data allow patterns with high angular resolution to be generated for specific wave modes that are identified using multi-dimensional Fourier transforms. The ability to study scattering as a function of both scattered angle and phase velocity also allows for better quantification and characterization of scattering phenomena than would otherwise be possible, which can be used to improve ultrasonic NDE methods and models.

In conclusion, this work has met its main research objectives and made a contribution to the field of ultrasonic NDE. Wavefield data was obtained for plates with through-holes of varying fill condition, which will aid in the verification of bulk wave modeling efforts. In addition, two methods for generating angle-beam scattering patterns for Rayleigh, shear, and longitudinal modes from wavefield data were developed, which can be generalized to obtain scatting information from any set of 3-D wavefield data.

7.2 Recommendations for Future Work

Although the work to date provides a means of estimating angle-beam scattering from through-holes in plates, a considerable amount of work is needed to improve the methods and apply them to additional experiments, which will inform future NDE methods and models. The remainder of this chapter is dedicated to providing specific recommendations for future work to improve and apply the signal processing techniques described in this thesis.

7.2.1 Improve Energy Mapping Methods

Both the radial and directional energy map methods successfully estimate scattering of each wave mode present in the wavefield, though additional work may improve each. Each method has issues in terms of separating the scattered wavefield from the incident wavefield, although to varying degrees. Baseline subtraction of wavefields in the time-space domain, developed by Dawson [17], can be used to reduce incident wave contributions. Processing the resulting residual wavefield through either method presented here would likely be more effective than baseline subtraction in their respective energy domains and may significantly improve results. Further improvements to the two methods should focus on providing techniques to separate incident and scattered waves when a suitable baseline wavefield is unavailable; to date, spatial windowing before processing with the directional energy technique appears to be the best method for isolating scattering above the hole.

7.2.2 Comprehensive Study of Fill Conditions

The main focus of this thesis was to provide a framework for estimating scattering from through-holes in plates using signal processing techniques; a small sample set of fill

conditions was tested to prove the validity of the proposed methods. Future experimental efforts should focus on acquiring wavefield measurements for a much wider set of fill conditions that simulate practical scenarios, which could include: complete filling with a more diverse range of metal and plastic fasteners, a larger set of couplants, and imperfect fasteners with defects such as corrosion, voids of various geometries, and partial sealants. Such experiments would provide a more comprehensive and informative view of the effects of boundary conditions on through-hole scattering.

7.2.3 Anisotropic Material Characterization

Although the radial and direction energy map methods were developed to estimate scattering from defects, both are applicable to other areas in ultrasonic NDE such as the characterization of anisotropic materials. In anisotropic materials, such as composites, the phase velocity of a particular mode is dependent on the direction of propagation. By attaching a piezoelectric transducer that produces ultrasonic waves propagating radially outward from the transducer to the surface of an anisotropic specimen, recording the wavefield, and processing with either method presented here, it would be possible to estimate phase velocity as a function of angle around the transducer, which provides information about velocity as a function of direction in the material of interest. Such characterization would provide the information necessary to extend NDE techniques used for isotropic materials to applications with anisotropic materials.

REFERENCES

[1] P. J. Shull, Ed., *Nondestructive Evaluation: Theory, Techniques, and Applications*. New York: Marcel Dekker, 2002.

[2] L. Rayleigh, "On waves propagated along the plane surface of an elastic solid," *Proceedings of the London Mathematical Society*, vol. 1, no. 1, pp. 4-11, 1885.

[3] H. Lamb, "On waves in an elastic plate," *Proceedings of the Royal Society of London. Series A*, vol. 93, no. 648, pp. 114-128, 1917.

[4] P. M. Shearer, *Introduction to Seismology*, 2nd ed. Cambridge, United Kingdom: Cambridge University Press, 2009.

[5] American Society for Nondestructive Testing, *Introduction to Nondestructive Testing* [Online] Available: https://www.asnt.org/MinorSiteSections/AboutASNT/Intro-to-NDT.

[6] Olympus Corporation, *Ultrasonic Flaw Detection Tutorial* [Online] Available: http://www.olympus-ims.com/en/ndt-tutorials/flaw-detection/

[7] A. J. Dawson, J. E. Michaels, R. M. Levine, X. Chen, and T. E. Michaels, "Acquisition and analysis of angle-beam wavefield data," in *AIP Conference Proceedings*, vol. 1581, pp. 1716–1723, 2014.

[8] M. V. Felice, A. Velichko, and P. D. Wilcox, "Accurate depth measurement of small surface-breaking cracks using an ultrasonic array post-processing technique," *NDT&E International,* vol. 68, pp. 105-112, 2014.

[9] J. Zhang, B. Drinkwater, and P. Wilcox, "Longitudinal wave scattering from rough crack-like defects," *IEEE Transactions on Ultrasonics, Ferroelectrics and Frequency Control*, vol. 58, no. 10, pp. 2171-2180, 2011.

[10] J. E. Michaels, T. E. Michaels, and B. Mi, "An ultrasonic angle beam method for in situ sizing of fastener hole cracks," *Journal of Nondestructive Evaluation,* vol. 25, no. 1, pp. 3-16, 2006.

[11] T. E. Michaels, J. E. Michaels, and M. Ruzzene, "Frequency-wavenumber domain analysis of guided wavefields," *Ultrasonics*, vol. 51, pp. 452-466, 2011.

[12] T. E. Michaels, J. E. Michaels, B. Mi, and M. Ruzzene, "Damage detection in plate structures using sparse ultrasonic transducer arrays and acoustic wavefield imaging," in *AIP Conference Proceedings*, vol. 760, pp. 938-945, 2005.

[13] X. H. Campman, K. van Wijk, J. A. Scales, and G. C. Herman, “Imaging and suppressing near-receiver scattered surface waves,” *Geophysics*, vol. 70, no. 2, pp. V21-V29, 2005.

[14] J. Takatsubo, B. Wang, H. Tsuda, and N. Toyama, “Generation laser scanning method for the visualization of ultrasounds propagating on a 3-D object with an arbitrary shape,” *Journal of Solid Mechanics and Materials Engineering*, vol. 1, no. 12, pp. 1405-1411, 2007.

[15] J. Blackshire, “Ultrasonic scattering from complex crack morphology features,” in *2012 IEEE International Ultrasonics Symposium Proceedings*, pp. 248-251, Oct 2012.

[16] The Collaboration for NDT Education: Iowa State University, *NDT Education Resource Center* [Online] Available: https://www.nde-ed.org.

[17] A. J. Dawson, *Acquisition and Analysis of Ultrasonic Wavefield Data to Characterize Angle-beam Propagation and Scattering in Plates*, Ph.D. dissertation, Sch. ECE, Georgia Inst. Tech., Atlanta, GA, 2015.

[18] H. Sohn, D. Dutta, J. Y. Yang, M. Desimio, S. Olson, and E. Swenson, "Automated detection of delamination and disbond from wavefield images obtained using a scanning laser vibrometer," *Smart Materials and Structures,* vol. 20, no. 0450127 (10pp), 2011.

[19] O. Mesnil, C. A. C. Leckey, and M. Ruzzene, "Instantaneous and local wavenumber estimations for damage quantification in composites," *Structural Health Monitoring,* vol. 14, no. 3, pp. 193-204, 2015.

[20] E. B. Flynn, G. S. Jarmer, S. Y. Chong, and J.-R. Lee, "Imaging and characterizing structural defects through the estimation of local dispersion curves," in *10th International Conference on Damage Assessment of Structures,* Dublin, Ireland, pp. 956-961, 2013.

[21] M. Ruzzene, "Frequency-wavenumber domain filtering for improved damage visualization," *Smart Materials and Structures,* vol. 16, pp. 2116-2129, 2007.

[22] Z. Tian and L. Yu, "Lamb wave frequency-wavenumber analysis and decomposition," *Journal of Intelligent Material Systems and Structures*, vol. 25, no. 9, pp. 1107-1123, 2014.

[23] Y. Al-Nassar, S. Datta, and A. Shah, “Scattering of Lamb waves by a normal rectangular strip weldment,” *Ultrasonics*, vol. 29, no. 2, pp. 125-132, 1991.

[24] Z. Chang and A. Mal, “Scattering of Lamb waves from a rivet hole with edge cracks,” *Mechanics of Materials*, vol. 31, no. 3, pp. 197-204, 1999.

[25] M. J. S. Lowe, R. E. Challis, and C. W. Chan, “The transmission of Lamb waves across adhesively bonded lap joints,” *Journal of the Acoustical Society of America*, vol. 107, no. 3, pp. 1333-1345, 2000.

[26] F. Lanza Di Scalea, P. Rizzo, and A. Marzani, “Propagation of ultrasonic guided waves in lap-shear adhesive joints: Case of incident A0 Lamb wave,” *Journal of the Acoustical Society of America*, vol. 115, no. 1, pp. 146- 156, 2004.

[27] Y. Lu, L. Ye, Z. Su, and C. Yang, “Quantitative assessment of through-thickness crack size based on Lamb wave scattering in aluminium plates,” *NDT&E International*, vol. 41, pp. 59-68, 2008.

[28] P. Fromme and M. Sayir, “Measurement of the scattering of a Lamb wave by a through hole in a plate,” *Journal of the Acoustical Society of America*, vol. 111, no. 3, pp. 1165-1170, 2002.

[29] O. Diligent, T. Grahn, A. Bostrom, P. Cawley, and M. Lowe, “The low-frequency reflection and scattering of the S0 Lamb mode from a circular through-thickness hole in a plate: finite element, analytical and experimental studies,” *Journal of the Acoustical Society of America*, vol. 112, no. 6, pp. 2589-2601, 2002.

[30] P. Fromme and C. Rouge, “Directivity of guided ultrasonic wave scattering at notches and cracks,” in *Journal of Physics: Conference Series*, vol. 269, no. 012018 (11pp), 2011.

[31] X. Chen, J. Michaels, and T. Michaels, “A methodology for estimating guided wave scattering patterns from sparse transducer array measurements,” *IEEE Transactions on Ultrasonics, Ferroelectrics, and Frequency Control*, vol. 62, no. 1, pp. 208-219, 2015.

[32] E. Glushkov, N. Glushkova, A. Ekhlakov, and E. Shapar, "An analytically based computer model for surface measurements in ultrasonic crack detection," *Wave Motion,* vol. 43, pp. 458-473, 2006.

[33] R. M. White, "Elastic wave scattering at a cylindrical discontinuity in a solid," *Journal of the Acoustical Society of America,* vol. 30, no. 8, pp. 771-785, 1958.

[34] L. Flax, V. K. Varadan, and V. V. Varadan, "Scattering of an obliquely incident acoustic wave by an infinite cylinder," *Journal of the Acoustical Society of America,* vol. 68, no. 6, pp. 1832-1835, 1980.

[35] A. Velichko and P. D. Wilcox, "A generalized approach for efficient finite element modeling of elastodynamic scattering in two and three dimensions," *Journal of the Acoustical Society of America,* vol. 128, no. 3, pp. 1004-1014, 2010.

[36] S. Das, S. Banerjee, and T. Kundu, "Elastic wave scattering in a solid half-space with a circular cylindrical hole using the Distributed Point Source Method," *International Journal of Solids and Structures,* vol. 45, pp. 4498-4508, 2008.

[37] J. Zhang, B. W. Drinkwater, and P. D. Wilcox, "Defect characterization using an ultrasonic array to measure the scattering coefficient matrix," *IEEE Transactions on Ultrasonics, Ferroelectrics & Frequency Control*, vol. 55, no. 10, pp. 2254-2265, 2008.

[38] J. Zhang, B. W. Drinkwater, and P. D. Wilcox, "The use of ultrasonic arrays to characterize crack-like defects," *Journal of Nondestructive Evaluation*, vol. 29, pp. 222-232, 2010.

[39] J. E. Michaels, S. J. Lee, A. J. Croxford, and P. D. Wilcox, "Chirp excitation of ultrasonic guided waves," *Ultrasonics,* vol. 53, pp. 265-270, 2012.

[40] A. J. Dawson, J. E. Michaels, and T. E. Michaels, "Isolation of ultrasonic scattering by wavefield baseline subtraction," *Mechanical Systems and Signal Processing*, vol. 70-71, pp. 891-903, 2016.